ABSTRACT

Title of Thesis: EXPERIMENTAL STUDIES ON DROPLET DEFORMATION IN HYPERBOLIC CONVERGING CHANNELS

Aditya Narendrababu Sangli,
Master of Science, 2017

Thesis Directed By: Associate Professor David I. Bigio,
Department of Mechanical Engineering

Using solid fillers to make composite materials in an additive manufacturing process has been extensively studied but there is no research on incorporating immiscible liquids in the process. To study this, a unique die was built which had a wall profile based on a hyperbolic equation and imposed constant extensional rate at the centerline. The deformation seen by a droplet of Castor oil immiscible in Silicone oil matrix was studied for various positions of injection into the channel using high speed imagery. Droplets injected at the center of the channel did not see any significant deformation while the droplets injected at an offset position stretched and reached the affine state. CFD simulations confirmed the existence of a strong shear effect closer to the walls. The results from this research will aid in understanding liquid filler behavior in a polymer flow and helps in incorporating liquids in polymer based additive manufacturing.

EXPERIMENTAL STUDIES ON DROPLET DEFORMATION IN HYPERBOLIC CONVERGING CHANNELS

by

Aditya Narendrababu Sangli

Thesis submitted to the Faculty of the Graduate School of the
University of Maryland, College Park, in partial fulfillment
of the requirements for the degree of
Master of Science
2017

Advisory Committee:
Professor David I. Bigio, Chair
Professor Richard Calabrese
Professor Amir Riaz

Acknowledgements

I express my sincere gratitude to Dr. David Bigio for being my mentor over the course of my graduate studies. I have learnt a lot from our conversations and it has constantly motivated me over the last two years to become a better version of myself. I appreciate your support and emphasis on my personal development on top of my progress as a scientist.

I thank Dr. Richard Calabrese and Dr. Amir Riaz for serving on my thesis committee and their expert contributions in improving my work.

I also express my regards to undergraduate colleagues Marcelo Arispe-Guzman and Connor Armstrong for assisting me in running the experiments. I appreciate your help with building the test rig and writing the image processing code. I would also like thank all my research colleagues at the Advanced Manufacturing Lab for their support.

Finally, I thank my parents for their guidance and having been a constant source of encouragement through the course of my studies.

Table of Contents

Page

List of Tables

List of Figures

Chapter 1: Introduction

Additive manufacturing, which had a humble beginning in the 1980s, is expanding into new avenues and new innovations and breakthroughs is the need of the hour to keep up with the ever expanding area. Popular additive manufacturing methods include Stereo lithography, Selective Laser Sintering and Fused Filament Fabrication. The latter, in specific, has seen vast improvements in ease of fabrication, cost to produce and is continuing to include a wide variety of new materials. Some of the most common desktop additive manufacturing machines use this method since the machines tend to be compact and is not labor intensive.

The popularity of Fused Filament Fabrication has attracted numerous researchers who aim to expand the range of print materials, strength of the printed part and print speed. Researchers have been successful in incorporating solid fillers into their raw material which makes the printed part a polymer composite. This resulted in improvements in strength, created a new avenue for subsequent research into incorporating multiscale composites and studying behavior of solid fillers in a matrix under a flow condition.

In order to contribute to increasing the versatility of polymer based additive manufacturing, incorporating liquid fillers and analyzing their behavior is the need of the hour. When liquids are incorporated into polymer based additive manufacturing, there is a potential to manufacture clear polymers that have channels of colored liquid embedded in them. The solid printed part can have an immiscible liquid embedded in it whose morphology can be controlled by process parameters of the additive

manufacturing method. This foray into a new area, using elements from prior research backed by a study of behavior of droplets in a matrix, has the potential to broaden the range of materials that can be processed using a polymer based additive manufacturing method.

1.1 Viscosity and Surface Tension

When a droplet of an immiscible liquid is suspended in a quiescent matrix, assuming absence of inertial effects, there are two forces in play – Viscous forces and Surface forces. The balance of these two forces causes the droplet to assume the most stable shape of a sphere. However, increasing the viscous forces will cause an unsteady effect on the droplet and it tends to move away from the shape of a sphere. Depending on the type of motion of the viscous matrix, the droplet has a tendency to deform in several different ways.

The surface forces cause the droplet to revert back into the spherical shape. This force, which is a function of the interface of the two immiscible liquids, results in interesting droplet morphologies when the viscous matrix is subjected to a flow field. Thus, the droplet morphology at any given time is a function of the balance between the viscous forces and the interfacial tension. A non-dimensional quantity called the Capillary number is thus formulated which takes into account the amount of deviation a droplet sees as well as the balance between viscous and surface forces.

1.2 Capillary number

The Capillary number represents the balance between the viscous forces and the interfacial tension. It is a function of the droplet size at any given instant (a), the rate of deformation instilled on the droplet ($\dot{e}$), viscosity of the matrix (μ) and the interfacial tension (σ) between the two interacting interfaces. As a formula, it is given by Equation 1.1.

$$Ca = \frac{a\dot{e}\mu}{\sigma} \tag{1.1}$$

Even though the magnitude of the rate of deformation is considered while calculating the Capillary number at given instant, the origin of this quantity is of vital interest since it can affect the droplet morphologies in different ways. Critical Capillary number refers to a stage where the droplet can no longer have a steady shape at the applied rate of deformation and will eventually breakup into daughter droplets. This phenomenon happens differently in different types of flows. Flows can be broadly broken down into a shear component and an extensional component.

1.3 Shear and Extensional Mixing

Mixing refers to reduction in scale of a component and its distribution over the matrix in which it is present. In the case of immiscible fluids, when the droplet phase experiences an increase in dimension along a direction, the dimension orthogonal to it will reduce due to volume conservation. This can be a method to achieve mixing of immiscible fluids and is evident from the formulation of emulsions which use the same principle. As a droplet elongates, it will achieve eventual breakup since the

surface forces will no longer be adequate to hold the phase together. From Equation 1.1, assuming a constant $\dot{e}$ over the process, it can be seen that the Capillary number associated with the droplet at a certain time goes down as the width reduces. The critical Capillary number at which breakup occurs is of tremendous interest since it can determine the point at which the transition from a single elongated droplet to a number of daughter droplets occurs.

Shear flow is depicted in Figure 1.1. There is a constant velocity gradient $\frac{du}{dy}$ associated with the flow. So when a droplet is subject to a shear flow, it behaves as shown in Figure 1.1. It can be clearly seen that a vorticity component is associated with the field since it causes the droplet to stray from a straight line path along the flow as it stretches. Many researchers have found the critical Capillary number for a shear flow to be around 0.4 when the viscosity ratio is one.

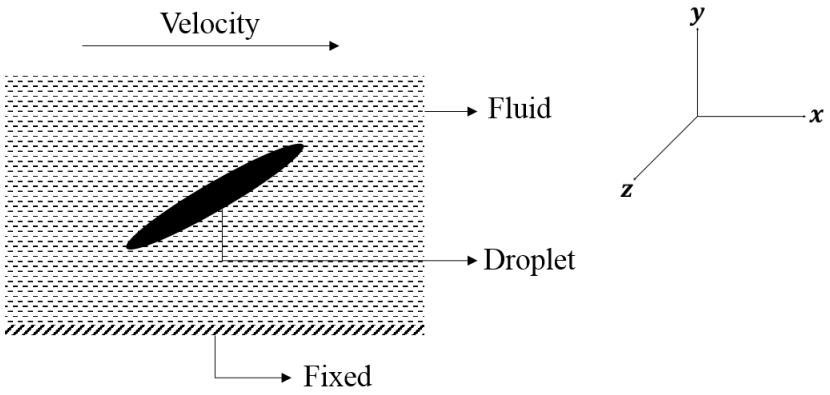

Figure 1.1: Schematic depiction of simple shear flow

On the contrary, a pure extensional flow is an irrotational flow. A schematic is depicted in Figure 1.2. The droplet simply stretches outward along both directions

causing eventual breakup. It does not stray from the line as it stretches and the critical Capillary number associated with the flow is about 0.2 when the viscosity ratio is one.

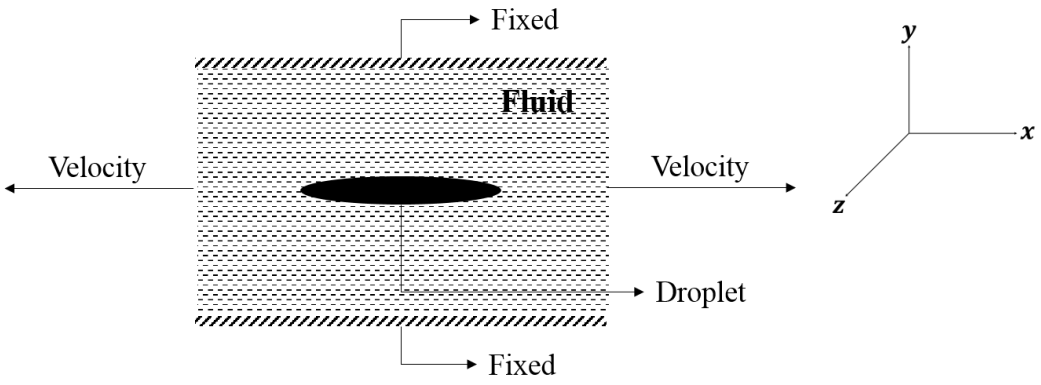

Figure 1.2: Schematic depiction of pure extensional flow

1.4 Applications

Incorporating droplet breakup principles into a manufacturing setup opens up avenues resulting in several novel applications.

1. Dies can be designed based on the type and degree of deformation needed on an immiscible droplet and incorporate it into an existing additive manufacturing setup
2. Liquid fillers can be incorporated into a polymer based additive manufacturing setup which results in additive manufacturing of interesting products like liquid filled solid parts
3. Channels for fluid flow internal to the part can be manufactured in situ in a dynamic additive manufacturing process

4. Transparent solid parts having a colored liquid flowing through them can be additively manufactured. Inspiration can be drawn from concepts like self-healing concrete which contain liquid concrete fillers at certain locations.
5. Some researchers have shown that parts can be stiffened by incorporating liquid fillers in them. Although there are material restrictions with such processes, the general idea can be used to develop stiffer parts which can have better shock absorbing capabilities.

1.5 Research Objectives

The objectives of this research are as follows:

- Develop a method to impose extensional deformation on an immiscible droplet which can be incorporated into a manufacturing setup
- Design and fabricate a channel for fluid flow which can impose an extensional deformation and subject an immiscible droplet at different initial Capillary numbers to track changes in Capillary number with position and time
- Study the effect of combined shear and extension on a droplet by injecting it at different offset positions in the channel to identify important factors which characterize the nature of deformation

1.6 Outline of the Thesis

The methodology used to achieve the objectives shortlisted is described in the following chapters of this thesis.

Chapter 2 presents a relevant and comprehensive literature review about the existing methodologies, concepts and results from the field of droplet deformation experiments.

Chapter 3 describes the methods used in the current study, the experimental design and the details about fabrication of an experimental test rig. The chapter also describes the experimental trials that were used to study the phenomenon.

Chapter 4 highlights the simulations performed and the solution schemes used.

Chapter 5 presents the results from the experiments and discusses the implications of the study.

Chapter 6 presents the conclusion from the current research and describes the future studies that must be performed to make the research comprehensive.

The **Appendix** A reports the code that was developed in order to post process images for scientific analysis.

The **Appendix** B shows the complete development of the velocity gradients along many lines and the calculation of the second invariant of the rate of deformation tensor.

Chapter 2: Literature review

2.1 Fundamental Droplet Formation and Breakup Theories

Lord Rayleigh [1] in 1879 did fundamental studies on breakup of a jet of water issuing from an orifice of a given shape. Previous researchers had observed that the cross section of the jet, taken at different distances from the orifice along the direction of propagation, had different profiles. This was attributed this to a capillary force and since the jet had a recurrent form while propagating, the phenomenon was attributed to the superposition of the vibrations of the fluid column on the general progressive motion. The vibrations were periodic and were proportional to velocity of the fluid exiting the orifice. Rayleigh performed experiments where different orifice shapes were considered and the wavelength of the observed vibrations was found to be proportional to square root of the pressure head. An analytical expression for the wavelength, as a function of the head of liquid and the area of cross section of the jet, was also found. Rayleigh further said that the degree of instability of the jet, which is a measure of the degree to which the jet breaks up, reaches a maximum when the wavelength equals 4.51 times the diameter of the jet. However, Rayleigh neglected the presence of a surrounding fluid, having a different viscosity, which imposes viscous forces on the jet causing instability and subsequent breakup.

Taylor [2] performed experiments where he subjected a droplet of known viscosity in a surrounding fluid having a different viscosity. Taylor used a "four roll mill" as shown in Figure 2.1, where different definable fields of flow can be produced by turning the wheels at different speeds and different directions. He also used a

"parallel band" apparatus which could produce shear flows. The immiscible droplet behavior was recorded and the length and width of the droplet was measured at various instances. The droplet shape was found to be consistent with the theoretical expression relating the deformation to the fluid parameters like viscosity and interfacial tension. The expression is given by the Equation 2.1.

$$\frac{L-B}{L+B} = F\frac{19\mu' + 16\mu}{16\mu' + 16\mu} \tag{2.1}$$

$$F = \frac{2C\mu a}{T}$$

Where L and B are the length and breadth of the droplet respectively. C is a parameter related to the strength of the flow, μ' is the viscosity of the droplet and μ is the viscosity of the surrounding fluid, a is the size of the droplet, T is the interfacial tension between the droplet and the matrix. However, Taylor failed to explain why the shear flow was unable to breakup droplets when the droplet viscosity was much higher than the matrix viscosity.

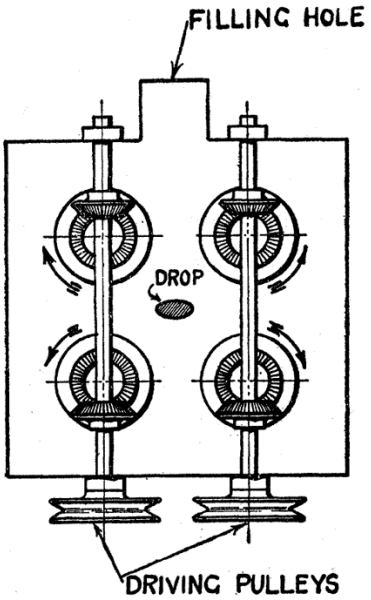

Figure 2.1: Four roll mill devised by Taylor [2]

Tomatika [3] correlated Rayleigh's and Taylor's observation of the behavior of a jet of fluid. He aimed to generalize the observations by solving the flow equations when a jet of a certain viscosity is subject to perturbations from a surrounding fluid, which results in propagation of the disturbance and jet breakup. He considered Taylor's observations when the viscosity ratio between the droplet and the matrix was a finite value, and found the wavelength at which the instability increases at the maximum rate resulting in droplet formation. His results, when applied to the case when the viscosity ratio is infinity i.e. a fluid of finite viscosity in a matrix with very low viscosity, validated observations of Rayleigh. Tomotika's research was the first to generalize droplet behavior in a matrix where the theory of propagation of a perturbation was assumed.

2.2 Droplets in Shear and Extensional Flow – Studies on Capillary Number

Grace [4] in 1971, in order to study the dispersion of immiscible droplets in a matrix, performed experiments with a four roll mill and subject droplets to shear flows and extensional flows. His application oriented research was particularly useful to generate an operating basis for mixing in plastic industries where dispersion of color concentrates is an objective. He generated vast amounts of data on time taken for droplet breakup to occur and maximum stable drop deformation for both shear and extensional flows and plotted them as a function of the viscosity ratio. One of the plots, shown in Figure 2.2, was of the ratio of the viscous forces to the interfacial forces at burst as a function of the viscosity ratio.

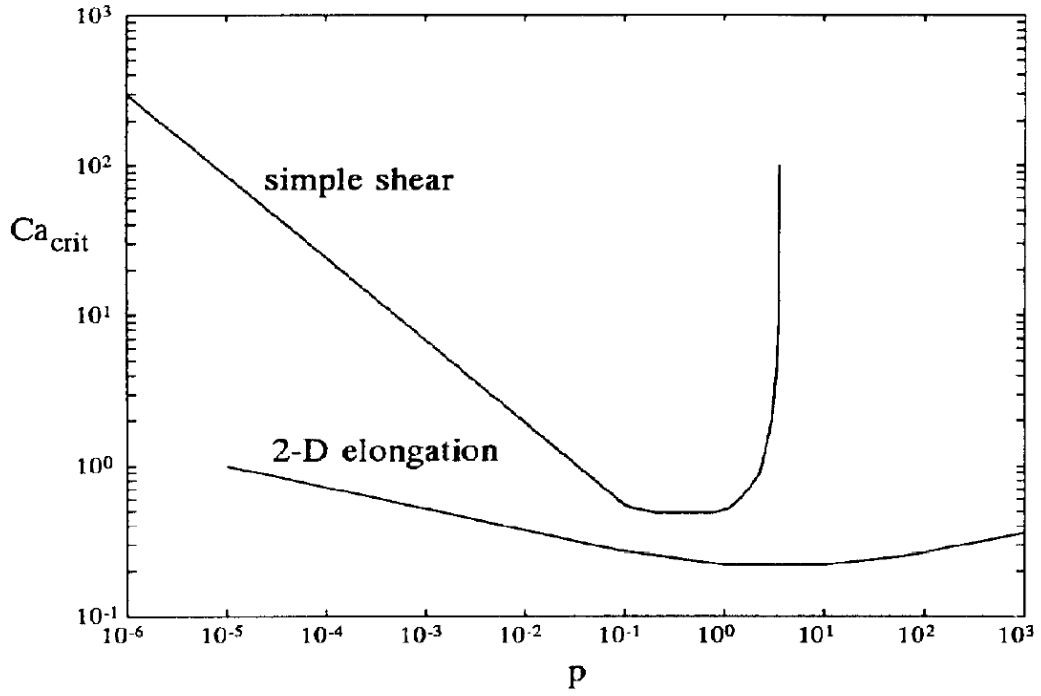

Figure 2.2: Critical Capillary number as a function of viscosity ratio for simple shear and 2D elongational flow [4]

Grace's research was one of the first to identify this quantity, termed as the Capillary number by future researchers, and it clearly showed the ability of each type of flow to produce droplets of a given size by virtue of the deformation induced. From the graph, it is evident that extensional flows can produce droplets of much smaller size compared to a shear flow subject to the same droplet conditions. It also shows how a shear flow is clearly inadequate to breakup droplets when the viscosity ratio increases beyond a certain limit. The plot validates Taylor's [2] observations where he mentioned that the "parallel band" apparatus could not breakup the droplet even when it was operating at the maximum possible speed. However, more recently, Stegeman et al.,[5] investigated the applicability of the curves in practical mixers. He argued that the initial shape of the droplet as well as the inhomogeneous conditions existing in a commercial mixer needs to be taken into account.

Bentley and Leal [6] did the next set of comprehensive experiments to generate the critical capillary number curve for a range of viscosity ratios. They performed drop deformation and burst experiments for viscosity ratios ranging from 0.001 to 100. The droplet viscosity ranged from 5 cSt to 60,000 cSt. They studied five different types of flows where the term α, which refers to the flow type (α = 1 being extensional flow and α = 0 being pure shear flow), ranging from 1.0, 0.8, 0.6, 0.4 and 0.2. From these comprehensive experiments, they were able to generate the critical capillary number curve. Critical capillary number refers to the state where the droplet can no longer have a stable profile when subject to the imposed flow. The droplet continuously undergoes deformation resulting in eventual breakup. The critical capillary number curve is shown in Figure 2.3.

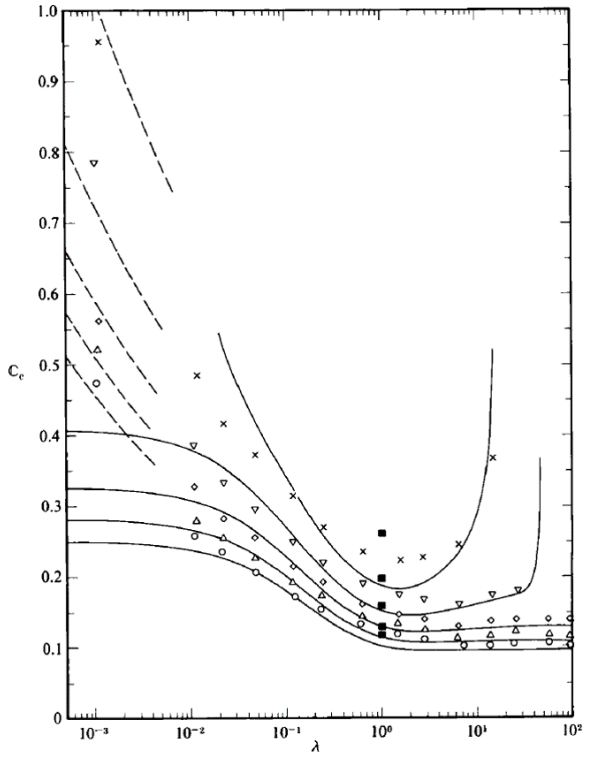

Figure 2.3: Experimental (symbols) and theoretical (lines) critical Capillary number for different flow conditions [6]

Rallison [7] summarized the findings of researchers over the years in the field of droplet breakup in shear and extensional flows. He stated that the external straining motion of the matrix promotes droplet deformation. The surface tension acts as a restoring force and inhibits this deformation. But due to conservation of volume, the droplet elongates and in the elongated shape, it aids further deformations. Rallison also summarized that low viscosity ratio drops can attain highly stable shapes whereas high viscosity ratio drops are pulled apart by modest extensional flows. These were further corroborated by Bentley and Leal [6] in their experiments. Stone [8] did another comprehensive review of the droplet deformation experiments and also provided a boundary integral scheme of predicting droplet shapes.

Marks [9] used a Couette device in his experiments where he found non-dimensional time associated with droplet breakup. Various plots of bulb onset time, initial breakup time and capillary onset time for various droplets were generated. These graphs are particularly useful since they provide a non-dimensional expression for time in terms of operating parameters and the geometry of the channel. For a shear flow, the bulb onset time graph obtained by Marks is as shown in Figure 2.4.

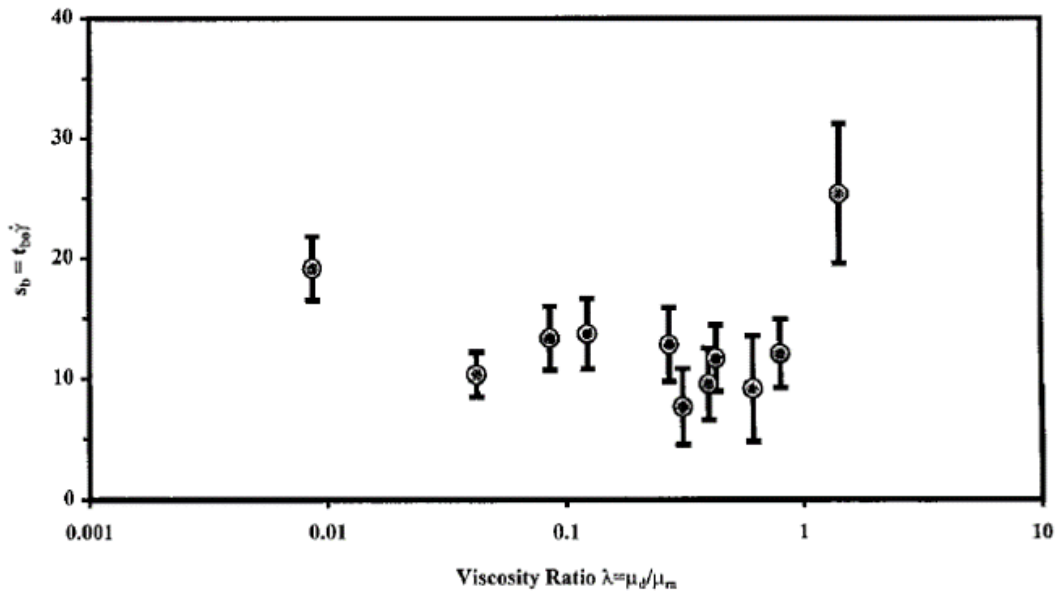

*Figure 2.4: Non dimensional bulb onset time (y axis) vs viscosity ratio (x axis). The bulb onset time is non dimensionalized as (bulb onset time * shear rate)* [9]

This graph can be useful to determine the characteristic time to droplet deformation in a Shear flow. Since both the axes are non-dimensional with respect to properties and flow strength, it can be useful to find the characteristic time associated with a Shear deformation of a droplet in any system.

He further observed a new type of deformation in his droplet breakup experiments and termed it as elongative end pinching. In this phenomenon, the ends of the droplet pinch off from the main thread and the main thread does not experience any retraction in length. This phenomenon occurs when the initial capillary number of the droplet is much higher than the critical capillary number of the type of flow and when it is continuously exposed to the shear field. Elongative end pinching was a new phenomenon not reported in the experiments of Stone et al., [10] who had investigated the transient behavior of stretched droplets after the flow was stopped.

2.3 Small and Large Deformation Theories

Taylor [2] assumed that the droplet deviated slightly from the spherical shape and was the pioneer of the "small deformation theories" to characterize droplet deformation. The velocity field inside and outside the droplet was found by the method of domain perturbations. Other researchers like Cox [11] have added higher order approximations to find the velocity field inside and outside the droplet and predict the shape. In the small deformation theory, the droplet surface is represented by a superposition of spherical harmonics of second and fourth order. However, this theory breaks down for highly elongated shapes which are especially possible in systems having a low viscosity ratio.

To address this, the large deformation theories were devised utilizing the fact that highly elongated shapes can be represented by a slender body. Buckmaster [12] presented a version of the slender body theory applied to droplet deformation. He commented upon the fact that the long droplet has a pointed end. In his slender body analysis, the droplet is assumed to be slender and its shape is represented by the Equation 2.2.

$$r = \epsilon R(x) \tag{2.2}$$

Where ϵ is the slenderness ratio defined by the Equation 2.3.

$$\epsilon = \frac{\sigma}{G\mu L} \tag{2.3}$$

The creeping flow equations were solved for both the inside as well as outside of the droplet which resulted in an expression for $R(x)$. Acrivos and Lo [13] independently derived Buckmaster's equations and applied volume conservation to obtain a

deformation relation. They commented on the state where the solution becomes unstable which is the point where the droplet bursts in the flow field around it. Theoretically, they estimated the dimensionless shear rate to be 0.148. This is close to the critical capillary number in an extensional flow of around 0.20 which was experimentally found by Grace [4] and other researchers.

2.4 Transient Deformation

When a stretched droplet is placed in a quiescent field, capillary waves which are present have a tendency to get magnified. Disturbances of many wavelengths exist and grow but one particular wavelength grows at the highest rate which leads to breakup of the thread.

Stone et al., [10] investigated the transient behavior of a stretched droplet in a general fluid flow. They used the same apparatus as Bentley and Leal [6] but stopped the four roll mill as soon as a certain aspect ratio was reached. They recorded the subsequent behavior of the stretched droplet in a matrix which was stationary. For different kinds of flows ranging from simple shear to pure extensional flow, a range of aspect ratios were found above which the droplet was found to breakup by the transient phenomenon. This plot is shown in Figure 2.5.

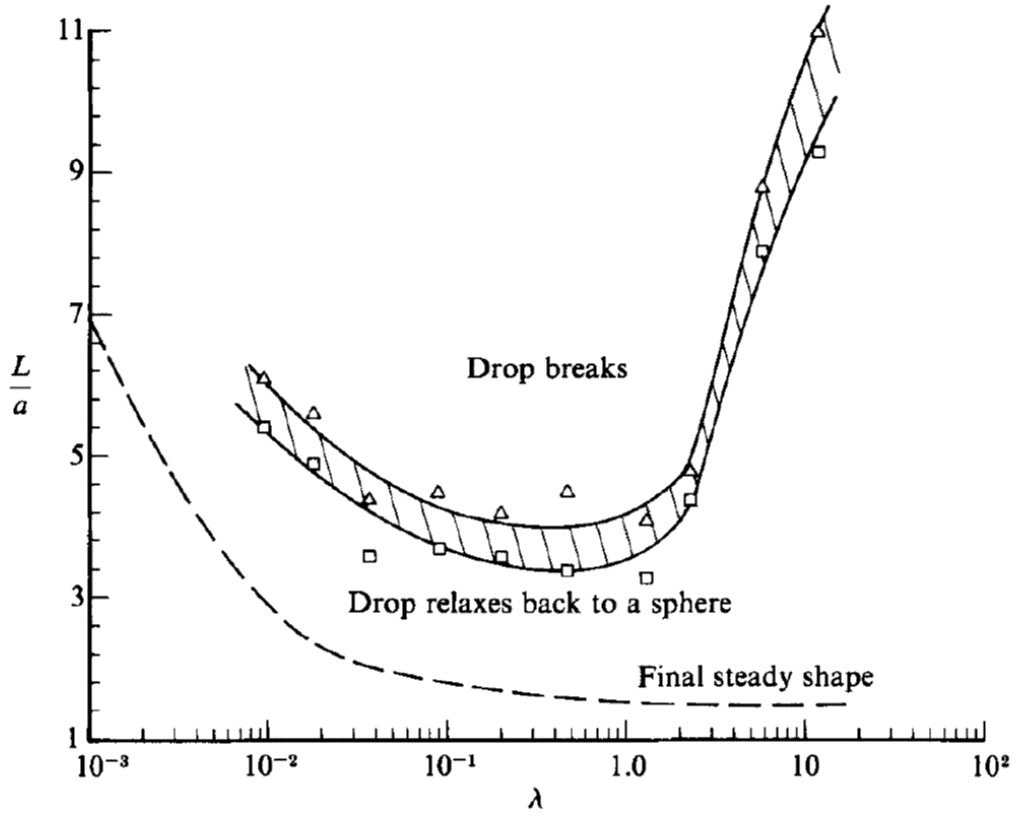

Figure 2.5: Critical aspect ratio of a droplet (hatched region) in a flow field to achieve transient breakup after flow cessation [10]

The plot can be used to design systems and formulate flow conditions so that deformation by the transient phenomenon can be obtained. Experiments by Ha and Leal [14] reported that the critical aspect ratio necessary to ensure droplet breakup after cessation of flow increases with increase in the Capillary number of flow. In other words, if Capillary number of the droplet is much higher than the critical Capillary number for the flow, the aspect ratio to which the droplet has to be stretched is higher than what was reported by Stone et al., [10]. This graph is shown in Figure 2.6.

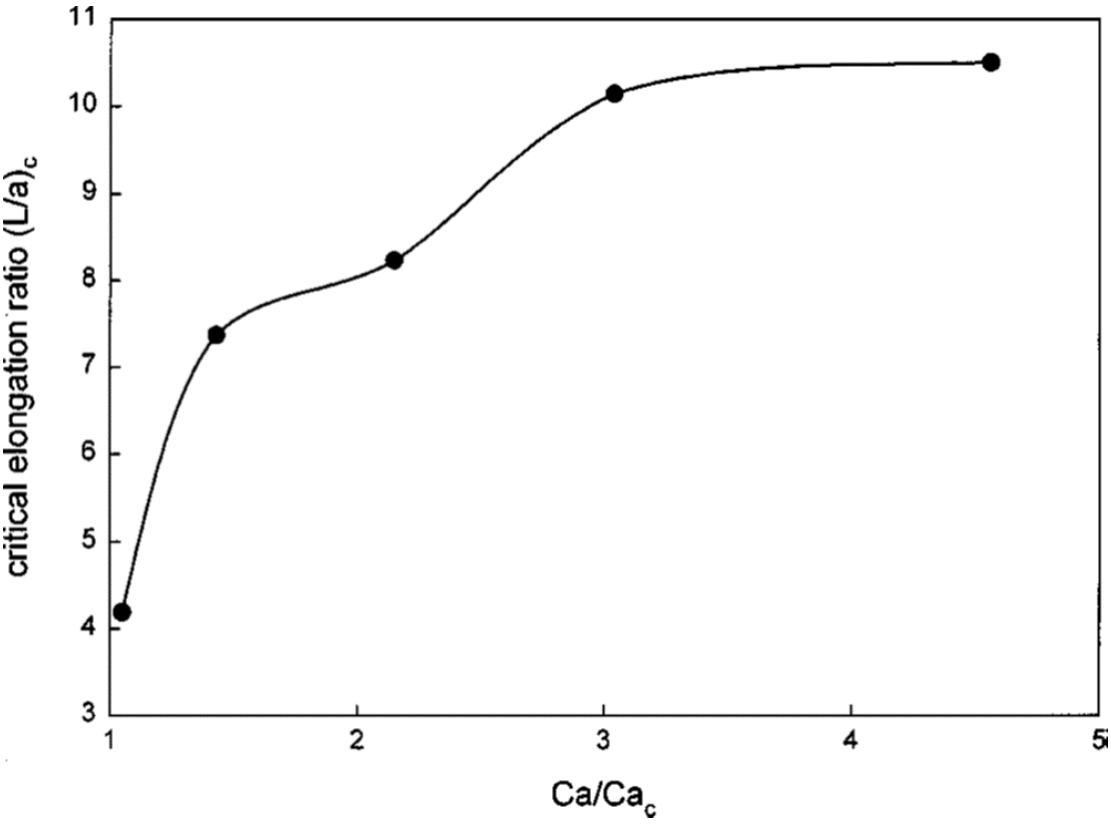

Figure 2.6: Critical elongation ratio dependence on the Capillary number of the droplets [14]

The graph shows that the aspect ratio necessary to ensure transient breakup scales with the Capillary number of the flow. So if a setup has to be designed that utilizes high Capillary numbers, the droplet has to be stretched to the appropriate aspect ratio before stopping the flow.

Experimental time to breakup of a droplet in a plane hyperbolic flow was studied by Janssen and Meijer [15]. They plotted the breakup time vs the $\eta_c \dot{e}/\sigma$ where η_c is the viscosity of the matrix (Silicone oil), $\dot{e}$ is the stretch rate imposed by the flow and σ is the interfacial tension between the droplet (Castor oil) and the matrix. This graph is shown in Figure 2.7.

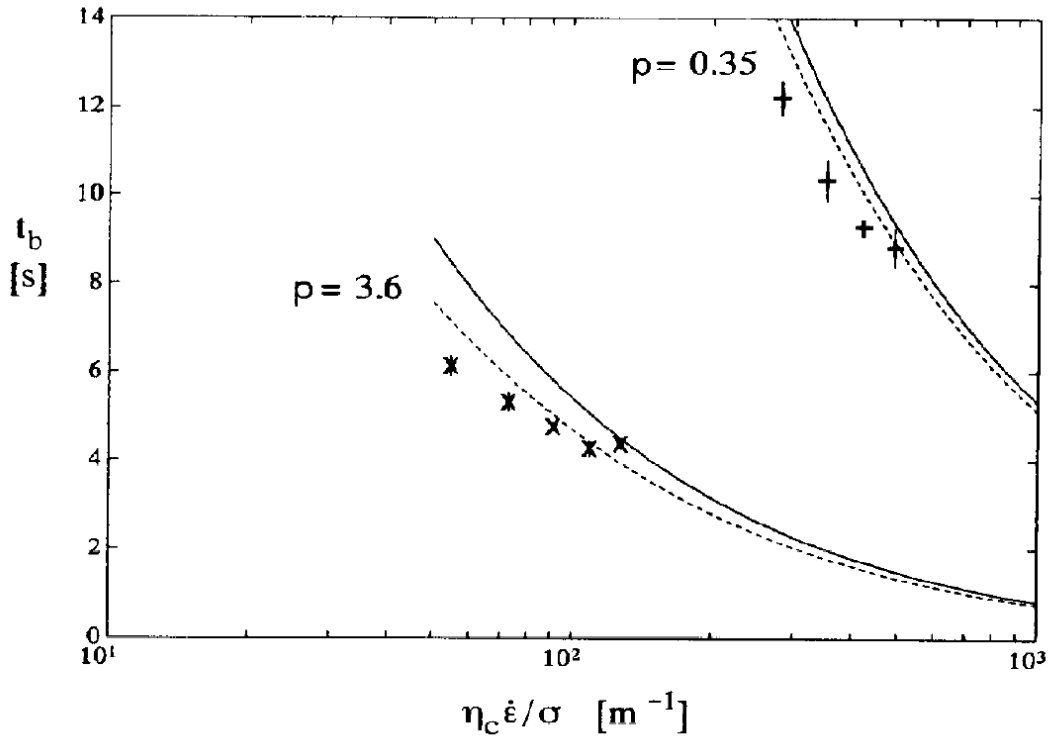

Figure 2.7: Experimental (symbols) and calculated (lines) droplet breakup time in a plane hyperbolic flow [15]

They even showed that the transient breakup phenomenon is much effective at producing smaller drops than a stepwise breakup phenomenon of the stretched droplet. The finest dispersion was not obtained when the viscosity ratio was unity but was obtained at a slightly higher value of the viscosity ratio.

2.5 Converging and Hyperbolic Flows

The seminal works of Taylor [2], Grace [4], Bentley and Leal [6], Stone et al., [10] and Janssen and Meijer [15] that aimed to model droplet breakup phenomenon all used a four roll mill to produce various definable fields of flow. However, this is not practical in a manufacturing setup and is purely an experimental device.

Chin and Han [16], Han and Funatsu [17], Godbille and Picot [18] and Bourry et al., [19] all used a converging channel to deform a droplet in their experiments. The converging action of the streamlines causes a volume element to undergo extensional deformation. They tested both Newtonian and Non Newtonian fluids. However, the extensional rate at the center of the channel, where the droplets undergo deformation, varies as the droplet moves down the channel. Since a steady extensional rate cannot be obtained, it is not possible to model the process assuming a constant extensional rate.

Oliveira et al., [20] devised a microfluidic channel that had walls based on a hyperbolic profile. They showed that the extensional rate can be made homogeneous along the centerline of the channel when the aspect ratio of the channel is low. Mulligan and Rothstein [21] used the theories to devise their own microfluidic hyperbolic channel shown in Figure 2.8.

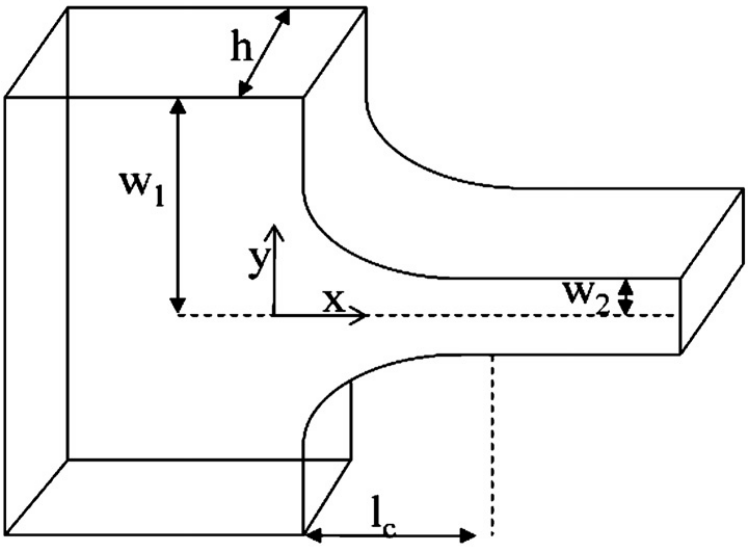

Figure 2.8: Schematic of the hyperbolic converging channel designed by Mulligan et al.,[21]

They provide a hyperbolic equation based on which walls can be designed in order to impose a certain value of constant extensional rate. This is given in Equation 2.4.

$$y = \frac{c_1}{x + \frac{2c_1}{w_1}} \tag{2.4}$$

c_1 is related to the geometry of the channel by Equation 2.5.

$$c_1 = \frac{1}{2} w_2 l_c \tag{2.5}$$

The extensional rate imposed along the centerline for this geometry is given by the Equation 2.6.

$$\dot{e}_{centerline} = \frac{\partial u}{\partial x} = \frac{Q}{c_1 h} \tag{2.6}$$

It can be observed from the equation that the extensional rate only depends on the flow rate (Q). The other terms are based on the geometry of the channel which remains constant. Thus, at different flow rates, different magnitudes of extensional rate can be obtained. This provides a basis to design channels based on which extensional deformation of droplets can be observed in experimental setups.

2.6 Scope of the Current Investigation

The four roll mill and the Couette device are some of the most commonly used experimental devices in droplet breakup experiments. It is a testament to their importance that standards set by Taylor [2], Grace [4], Stone et al., [10], Bentley and Leal [6] among other researchers, who all used a four roll mill, have been widely accepted as a starting point for many other studies. However, a four roll mill is not

particularly useful in a manufacturing setup where the droplet breakup phenomenon can be used to produce interesting internal morphologies in a fabricated part.

This research work is one of the first steps in incorporating flow effects produced in a hyperbolic channel in order to breakup immiscible droplets. Oliveira [20] and Mulligan and Rothstein [21] have used hyperbolic channels in microfluidic applications but have been mostly restricted by virtue of the inherent assumptions including low flow rates and are expensive to fabricate. They focused on confinement induced shear and did not investigate the effect of the flow on slender droplets in the channel.

In any conventional manufacturing setup, the hyperbolic channel can be incorporated to impose an extensional deformation on the immiscible droplet which can lead to elongated shapes. Additive manufacturing dies can be fabricated, which have hyperbolic wall profiles, and the preliminary results from this research can be used as a starting point to incorporate immiscible liquids in the process to produce interesting profiles and liquid filled channels.

Chapter 3: Experiments

3.1 Materials

In this experimental study, the matrix phase used was Silicone oil and the droplet phase was Castor oil. The properties of each are mentioned in the Table 3.1.

Table 3.1: Summary of fluid properties

Liquid	Viscosity (cSt)	Interfacial tension (N/m)
Polydimethylsiloxane	1,000	0.004
Castor oil	600	

Polydimethylsiloxane, which is the chemical name of Silicone oil, was procured from Consolidated Chemical and Solvents LLC. Silicone oil was used as a matrix liquid because it is optically clear and is available in a range of viscosities. Silicone oil was also the popular choice of the matrix fluid among the research groups of Mikami et al., [22] and Janssen and Meijer [15]. This allows the deformation of the droplet phase to be photographed easily and does not stain the apparatus.

Commercially available Castor oil was used in the experiment. The interfacial tension between Silicone oil and Castor oil was reported to be 0.004 N/m by Janssen and Meijer [15] and this value was used to perform the preliminary calculations.

3.2 Design of the Channel

An experimental channel having a rectangular cross section was designed. A rectangular cross section ensures that the Reynolds number remains constant through

each section and is easier to construct than an axisymmetric channel. The depth of the channel (Dimension into the plane) at each section was held constant at 20 mm. The channel is divided into three sections. The first section, having a length of 70 mm, is for the motion of the plunger which pushes the bulk liquid into the converging zone at a given inlet velocity. The second section, having a length of 40 mm, is the converging zone where there is an extensional flow. The third section is a long, straight zone which leads to the outlet. The 2D view of the channel is shown in the Figure 3.1.

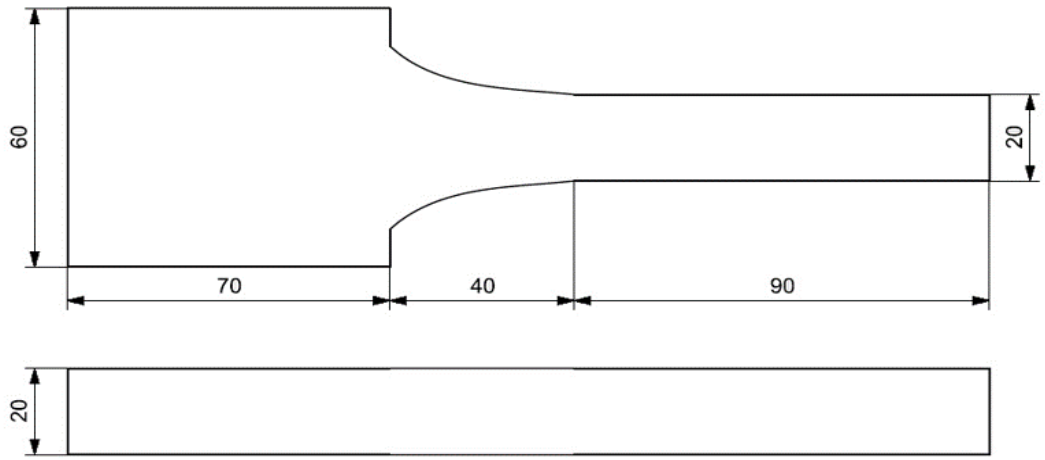

Figure 3.1: Front view and side view of the hyperbolic converging channel

The converging zone design is based upon the equations from Mulligan and Rothstein [21]. In their research, the extensional rate and the flow rate in the channel was related by the Equation 3.1.

$$\dot{e} = \frac{2Q}{wLh} \tag{3.1}$$

Where *'w'* is the downstream half width of the channel, *'L'* is the length of convergence, *'Q'* flow rate in the channel and *'h'* is the depth of the channel. Since

the only independent variable in the equation is the flow rate, for different inlet velocities, different extension rates can be obtained.

The equation of the wall profile, shown in Equation 3.2, of the converging zone is a hyperbolic equation

$$y = \frac{600}{3x + L} \tag{3.2}$$

Where 'L' is the length of the converging zone. The profile was plotted and fit between channel half widths of 30 mm inlet and 10 mm outlet.

3.3 Construction

The channel, based upon the designed values, was fabricated using Acrylic. Various methods and auxiliary parts were used to implement the designed experiments in the channel.

3.3.1 Fabrication of the Channel

Acrylic, commonly referred to as Plexiglas, was procured in the form of sheets that were 5 mm thick. The front view of the channel profile shown in Figure 3.2 was drawn in a CAD software (Unigraphics NX 11) and was converted to a file format suitable for the laser cutting machine (Universal Laser Systems 5mW CO_2 laser). Four such sheets were laser cut and stacked upon one another, resulting in 20 mm depth of the channel, to make one half of the channel. The other half was fabricated in a similar way and each half was positioned on a sheet with the appropriate amount of gap between them to make up the full assembly.

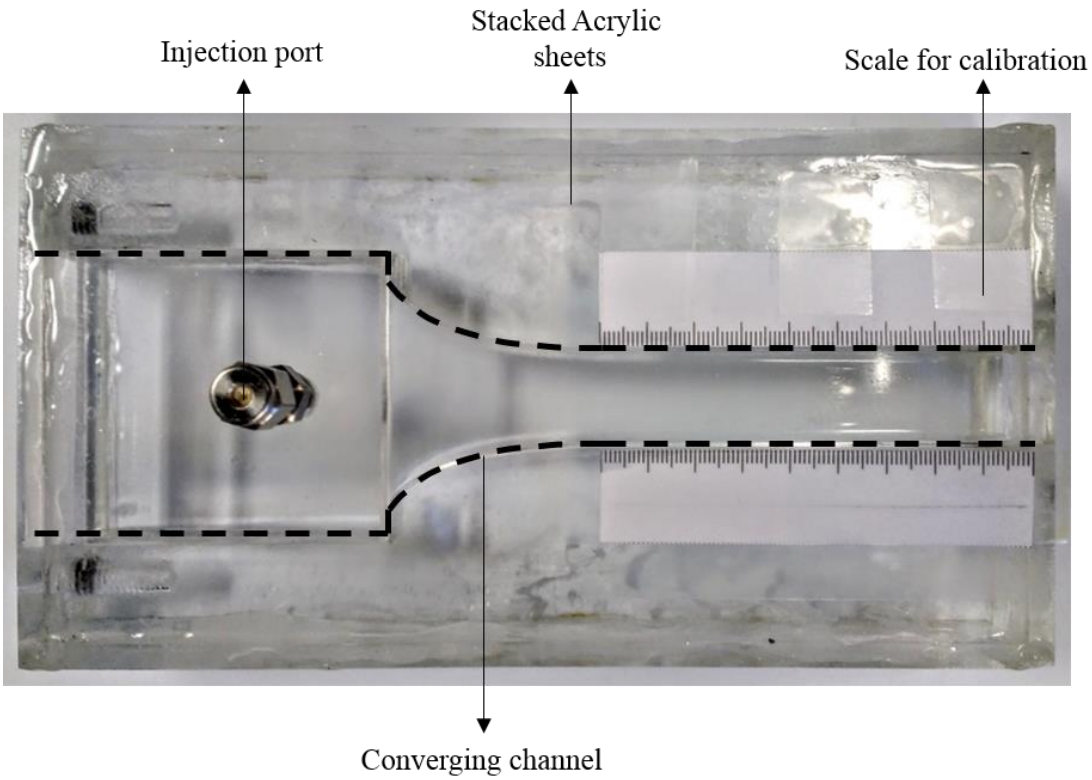

Figure 3.2: Hyperbolic channel fabricated with Acrylic sheets

3.3.2 Injection Port

At a distance of 55 mm from the top of the channel, a 1/8" NPT hole was tapped in order to accommodate the injection port. This injection port was a pipe fitting (SS-200-1-2BT) procured from Swagelok which had an internal assembly comprising of a ferrule set and a rubber septum. The rubber septum, procured from Sigma Aldrich, allowed for multiple rupturing and healing whenever a syringe was forced through it.

3.3.3 Supports

The channel was held vertical using an assembly of Aluminum 80 X 20 tubes shown in Figure 3.3. Two Acrylic plates were also attached to the assembly which helped to accommodate the plunger and guide it through the channel inlet.

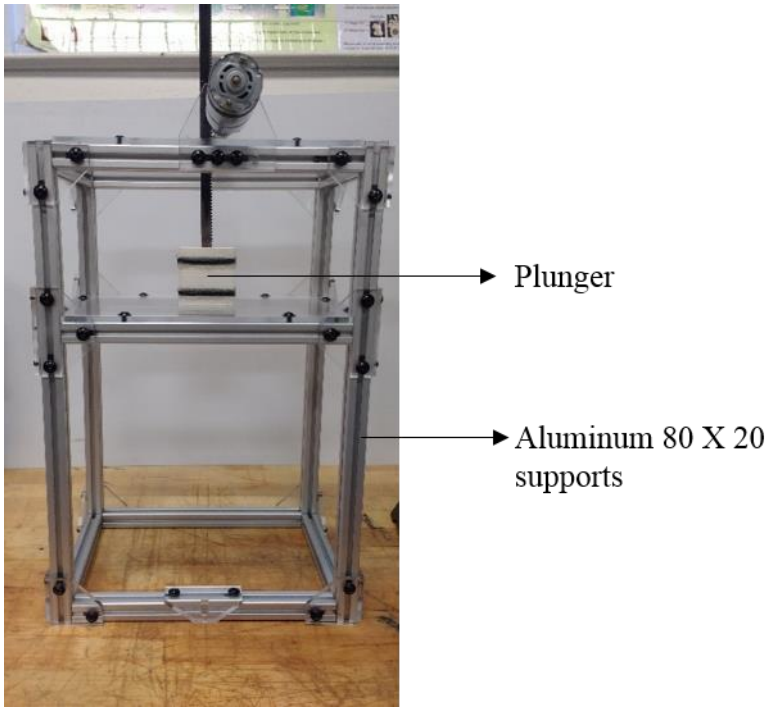

Figure 3.3: Supporting structure for the channel fabricated using 80 X 20

3.3.4 Plunger

The plunger, which pushed the fluid through the channel at a known velocity, was fabricated by a Fused Deposition Modelling process. The plunger was designed on Unigraphics NX 11 and was converted into an STL file to be 3D printed. There were several allowances on the design in order to allow for assembly of a dual O-ring setup and the rack gear. A bleed port, which was essentially a hole running from the top to bottom, was also built into the plunger and could be sealed with a rubber stopper. This was necessary to remove any air that was trapped between the plunger and the oil before the commencement of the experimental trials.

3.3.5 Rack and Pinion Assembly

A rack and pinion assembly was used to drive the plunger up and down the channel. They were held in position using the Acrylic sheet on the support. The rack gear (RGEA 1.0-300-ST) and the pinion gear (GEAB 1.0-22-10-B-6) were procured from Misumi and the pinion was driven by a DC 12V motor (ZYT555). The plunger was attached to the end of the rack. The assembly is shown in Figure 3.4.

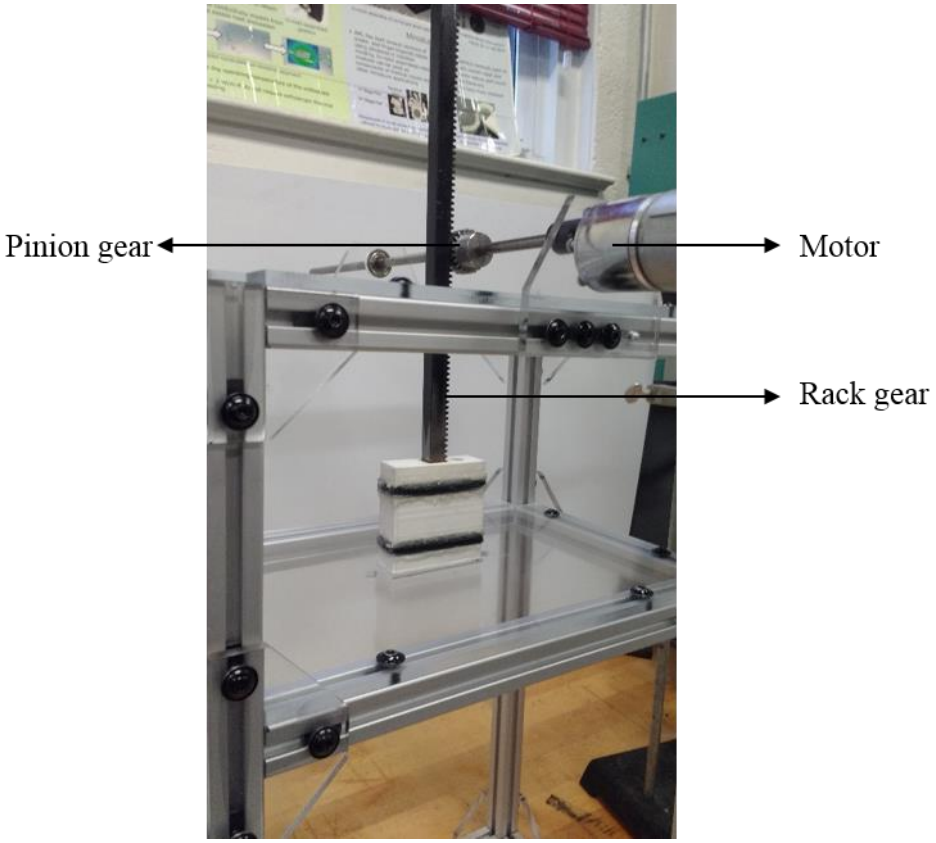

Figure 3.4: Rack and pinion assembly

3.3.6 Outlet

The outlet was channeled into a flexible pipe using a 3D printed coupling. The pipe was routed above the channel and was suspended at a height greater than the height of the whole apparatus. This allowed the liquid level to be the same in the channel and

in the outlet pipe. Thus, the liquid remained static in the channel even though the device was vertical and flowed out at the input velocity only when the motor was turned on.

3.4 Speed Control

The calculated inlet velocities can be produced by moving the plunger at different speeds. This was made possible by using an Arduino Uno board which controlled the motor driving the pinion gear. The required PWM value, which can be set on the computer controlling the Arduino, was input to the Arduino which translated to a calibrated value of the motor speed. The graph of output speed of the plunger vs. PWM setting on the Arduino is shown in Figure 3.5.

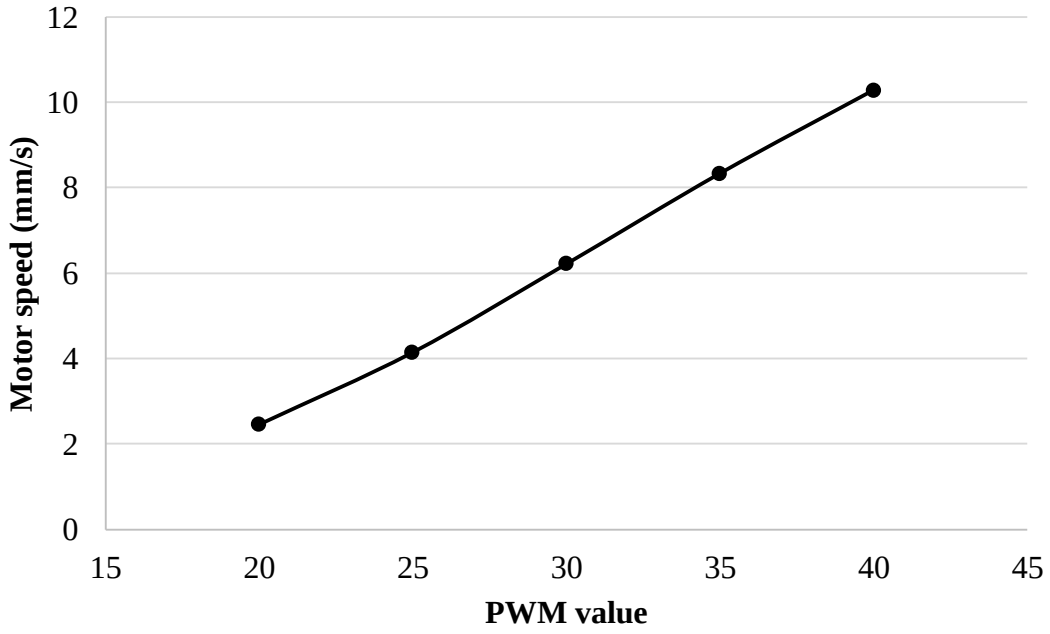

Figure 3.5: Plot of motor speed (mm/s) vs. PWM setting of the Arduino

3.5 Photography Setup

All the components of the system were assembled and the optimum position for placement of the camera was found. Lighting forms an important part of any image acquisition setup and two LED arrays were used. They were placed on either sides of the experimental apparatus and were focused towards the white background in a spot facing the center of the converging channel. When oriented this way, the two light sources created a halo around the castor oil drop which made the droplet well defined in the flow field. This arrangement was used as a standard for all the subsequent experiments and the schematic is shown in Figure 3.6.

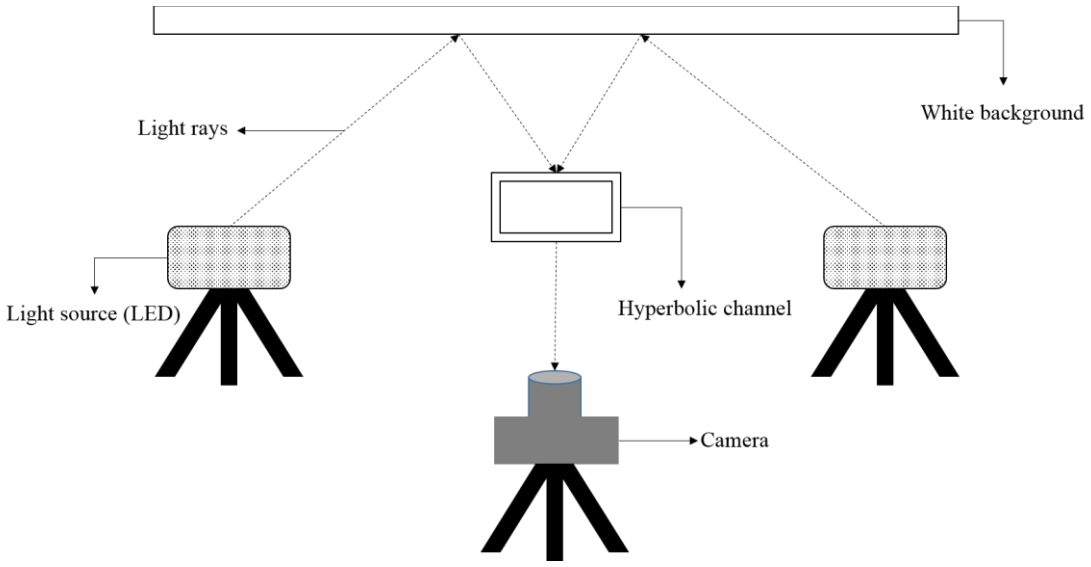

Figure 3.6: Schematic of lighting and camera setup (Top view)

A variety of image acquisition techniques were implemented. Initially, high speed videos were taken at around 60 frames per second and individual frames were extracted from it. A machine vision camera (Chameleon3 by FLIR) was used for this purpose. However, the maximum resolution that could be obtained was 1280 X 720

pixels and in order to improve the resolution with an acceptable reduction in frame rate, a different camera was used.

For this, the Nikon D7100 was used and images were taken at 6 fps. The camera produced images at 6000 X 4000 resolution where the droplet phase could be seen with incredible detail. High resolution images were required in order to implement the image processing algorithms on MATLAB.

3.6 Post Processing Images

The series of images from a single experimental trial is subject to post processing to extract the droplet dimensions in various positions in the channel.

3.6.1 Image enhancement

The selected frames for image enhancement include the initial droplet before it enters the converging channel and a series of images as the droplet travels down the channel before exiting. The frames are imported into Adobe Photoshop CC, an image altering software, where they are enhanced. A new layer is created for every imported frame and is placed directly above the original image. On this layer, the drop is traced using the Pen tool. Curves along the drop are approximated using the tool and once the outline of the drop has been traced, it is selected and filled black using the Paint tool. Next, the layer of the frame is hidden and the resulting black drop on a white background is exported as an image file with the same resolution as the source image. This process is repeated for the remaining range of frames for a single experiment and subsequently for all the other experiments.

In this process, drops are traced by hand rather than using in built algorithms due to the high image resolution which makes droplet features well defined. The halo created by the two light sources also helps to define the drop's profile when tracing. For this reason, manually tracing the drop using Photoshop gives an accurate representation of the drop.

3.6.2 Image processing in MATLAB

All the enhanced images are exported to MATLAB where the saved program, listed in the appendix, is run. The program begins by reading an image using the imread() function. This creates an array in MATLAB which represents the pixel information of the source image. The image type is then changed from a grayscale image (0 to 255 pixel values) into a binary image (0 and 1 pixel values) using the rgb2gray() and im2bw() functions. This gives a scheme to differentiate the black droplet image from the white background as shown in Figure 3.7. A final imcomplement() function is used to invert the image since MATLAB can only analyze white portions (having a pixel value of 1) of an image. The function bwconncomp() can now be used to

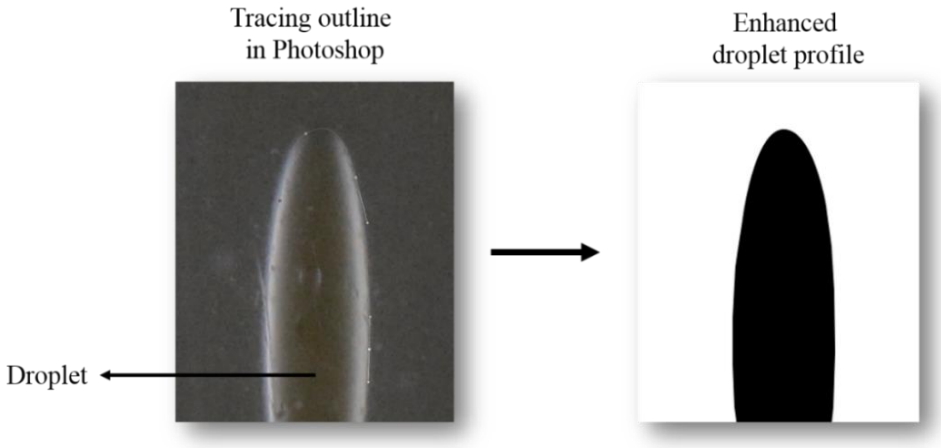

Figure 3.7: Image enhancement summary

separate connected parts in the image and obtain information such as Area, Centroid, Bounding Box, and Eccentricity. In addition to these properties, the diameter of the droplet along its longitudinal axis is obtained using a series of for-loops to determine the diameter at every pixel in the *y* direction. These properties are obtained for every frame for the trial and is kept in lists, which are to be exported from MATLAB into an Excel file.

The process is then repeated for every trial. The MATLAB program can be used for any droplet image created in Photoshop CC and the only parameters that are required are the date, the trial number, the number of images that are in the folder, and the image size.

In order to translate pixel data into dimensional units, the size (in mm) to pixel ratio is needed. This data is specific to each trial since it depends on the position of the camera and the magnification. For each trial, a test image is opened in MATLAB and the number of pixels between the walls of the channel is counted. Since this is a constant width, the size (in mm) to pixel ratio is calculated. The final steps of post processing include tabulating the data in the required format in the Excel file and plotting the relevant graphs.

3.7 Experimental Methods

The flow channel was attached to the support and was filled with Silicone oil till the level of oil in both the channel and the outlet pipe were the same. This made the system to be stable. The bleed port on the plunger was opened and the plunger was pushed into the channel till it just made contact with the oil. Air escaped from the

space between the plunger and the oil and the bleed port was sealed with a rubber stopper after all the air escaped. The channel was now ready to receive the droplet phase commence the experiment. Castor oil, being the droplet phase, was filled into a syringe which dispensed it through a two inch long 20 gauge needle. Many needles were cut to the required lengths so that the droplet could be injected at different positions into the channel. The needle was made to pierce the rubber septum on the injection port and the droplet was dispensed into the apparatus. Each division on the syringe was equal to dispensing a drop having a diameter of 2.67 mm which was found by volume conservation calculations. However, precise control of the position was not possible. This problem was not a major concern since the diameter was converted to an equivalent capillary number which was calculated using the inlet speed, whose control was easier.

After dispensing the droplet, the needle was withdrawn. The droplet was moved slowly towards the converging zone till it came into view of the camera. The plunger was stopped and at this point, a photograph was taken to measure the initial diameter of the droplet. The high speed setting was turned on in the camera and the plunger was moved at the designed speed. Multiple images of the droplet were taken as it passed through the converging zone. The plunger movement was stopped when the droplet moved away from the view of the camera. These images were stored separately and were subject to post processing. The motion of the plunger was reversed so that it could be removed from the channel. The residual droplet phase was then removed from the channel using a bigger syringe to suck out any residual

droplets. Silicone oil was then refilled in the channel and it was ready for another experimental trial.

For this research, experiments were performed for capillary numbers much higher than the critical capillary number for an extensional flow (around 0.2). The focus was to observe the various deformation mechanisms in the converging region for different positions of deployment.

3.8 Experimental Trials

For the preliminary experiments, the droplets were injected in the center of the channel to observe the changes in capillary number when subjected to the flow. Since the droplet size was not accurately controllable, a range of initial Capillary numbers much higher than the critical Capillary number for an extensional flow was produced. The flow was filmed with the high speed camera and Photoshop was used for subsequent frame extraction and image processing. Table 3.2 shows the operating conditions for this set of experiments.

Table 3.2: Operating conditions for center deployment experiments

Arduino PWM setting	**Plunger speed (mm/s)**	**Initial drop size (mm)**
100	34.08	3.10
120	42.02	2.77
140	49.96	3.10
160	57.90	2.61
180	65.84	2.52
200	73.78	2.65

In order to see the effect of changing the location of droplet injection, some droplets were injected at different distances along the *z* axis from the center so that combined shear and extension effects could be observed. In order to reduce the number of variables affecting the analysis, all experiments were run at 34.08 mm/s. Table 3.3 shows the experimental conditions.

Table 3.3: Operating conditions for offset deployment experiments

Arduino PWM setting	**Plunger speed (mm/s)**	**Distance from center (mm)**	**Initial drop size (mm)**
100	34.08	-1.0	3.17
		-2.0	3.58
		-6.0	3.39
		+6.0	3.73
		-7.5	3.41

Chapter 4: Simulations

The fluid flow in the hyperbolic channel cannot be approximated to a 2D channel flow ($z = 0$) since the droplets were injected into the Z-plane at different positions and the shear effects played a significant role in deforming them. The 3D flow equations are very complex in the hyperbolic channel and White [23] addresses the analytical solution for the velocity in the upstream rectangular duct. However, the effect of the convergence is not accounted for. Since there was no framework available to calculate the rate of deformation tensor along each streamline, simulations of the single phase channel flow was performed using ANSYS Fluent, Academic research, Release 17.2.

ANSYS Fluent performs Computational Fluid Dynamics simulations in order to solve the characteristic flow equations. The flow in the hyperbolic channel is a low Reynolds number, viscous, incompressible flow. Gravity is also accounted for since the channel is oriented in the vertical direction. The 3D geometry is divided into a large number of hexahedral elements and the conservation equations are computationally solved for each element. Post processing can be done in order to extract the velocity, pressure field and its derivatives. Gradients of the velocity field can be calculated along any streamline and each quantity can be compared to find the relative effect on a droplet placed in the field.

4.1 Method and Procedure

The CFD methods involve construction of the geometry, discretization of the flow field, setting up fluid properties and imposing the boundary conditions before solving the flow equations.

4.1.1 Geometry

The 3D geometry of the flow channel was modelled in Unigraphics NX software and then imported into ANSYS Fluent design modeler. Figure 4.1 shows the isometric view of the geometry. The dimensions are the same as shown in the schematic in Figure 3.1 and the dimension in the *z* direction is 20 mm.

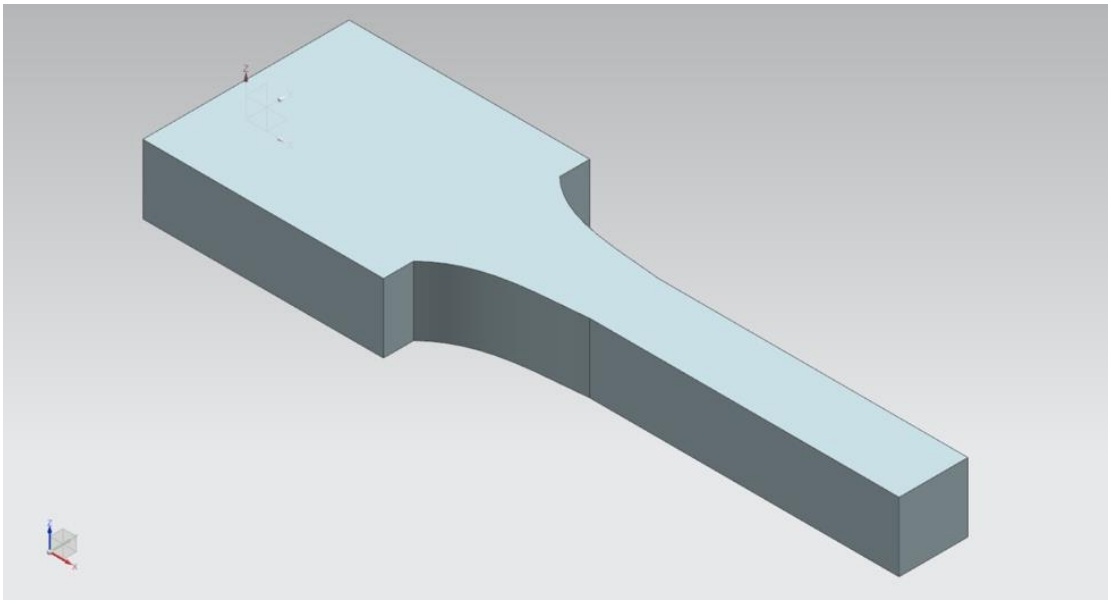

Figure 4.1: Geometry of the hyperbolic channel used for CFD simulations

4.1.2 Meshing

The geometry is divided into hexahedral elements and the mesh is shown in Figure 4.2 and Figure 4.3. It is a structured grid with 378,000 hexahedral elements.

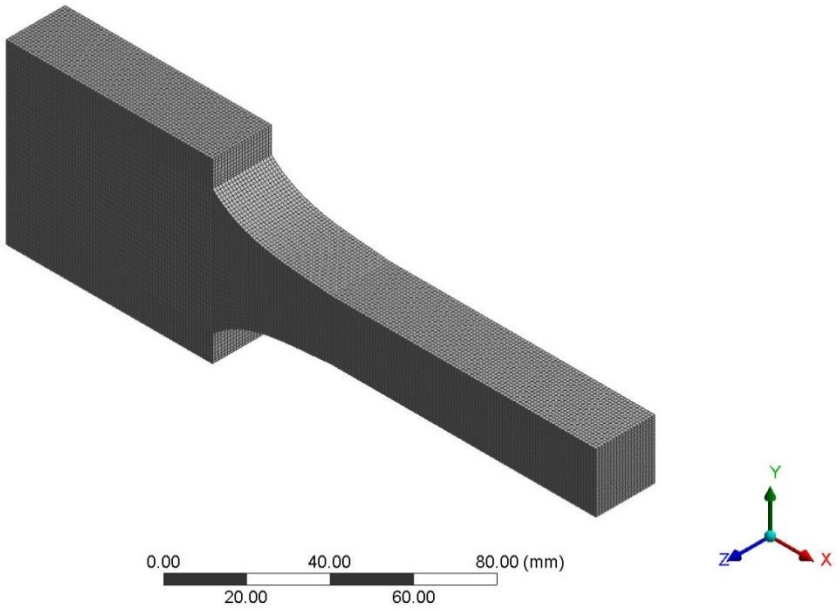

Figure 4.2: Isometric view of the mesh.

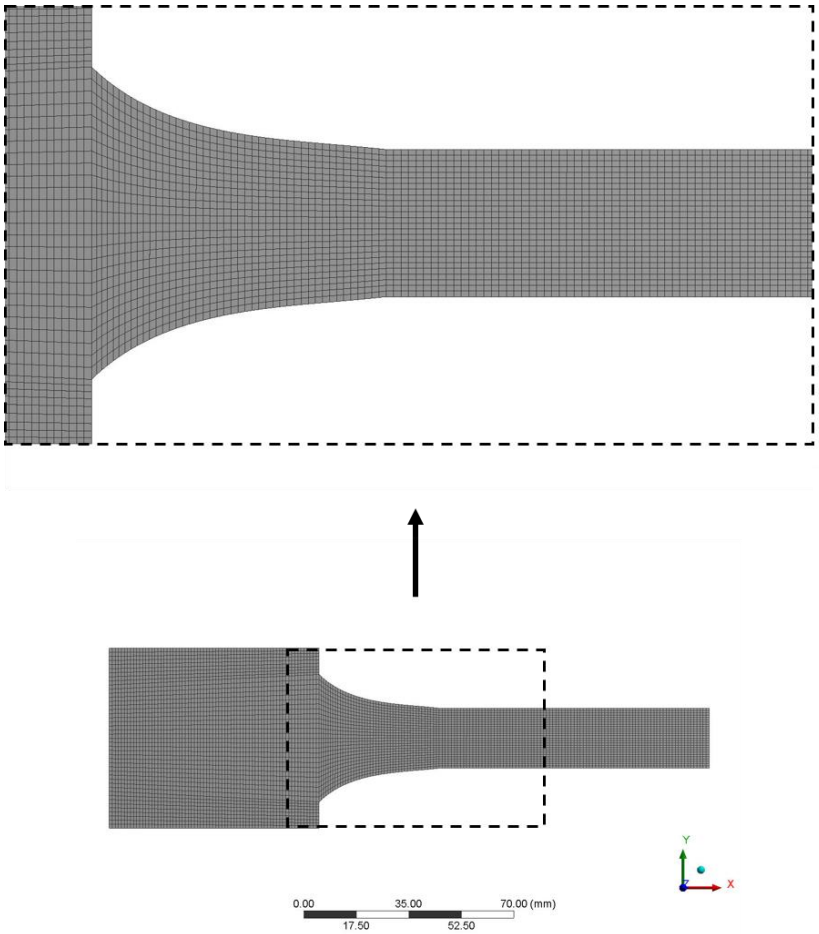

Figure 4.3: Front view of the hexahedral mesh with exploded view of the hyperbolic section

4.1.3 Boundary Condition

The inlet face measuring 60 mm X 20 mm is given an inlet velocity boundary condition, corresponding to the velocity of the plunger. This value can be changed across each trial and set to the speed at which the plunger is moving.

All the walls are given a no slip boundary condition. The outlet measuring 20 mm X 20 mm is open to the atmosphere, through the outlet pipe, and is given a pressure-outlet boundary condition equivalent to the atmospheric pressure.

4.1.4 Solution

For the CFD simulation, the Semi-Implicit Method for Pressure Linked Equations (SIMPLE) scheme of solution is chosen. The residual value is set to 10^{-5} for convergence of the solution.

4.1.5 Post Processing

ANSYS Fluent has an interface which can output contour plots, vector plots and path lines among other data. Further, XY plots of the three components of velocity along any given line in the streamwise direction can be obtained.

4.2 Results

The velocity components of flow at any plane or along any line in the flow field can be obtained by post processing the computational data. Since the objective of this research is to understand the behavior of droplets injected at different positions in the channel, the velocity gradients at those points need to be found.

4.2.1 Velocity profile

The velocity profile can help in understanding the behavior of the fluid flow along different planes. A sample set of results are discussed for an inlet speed of 34 mm/s. The profile is parabolic along both *y* and *z* axes and it develops as shown in Figure 4.4. The '*u*' component of velocity is dominant and v and w components are almost negligible.

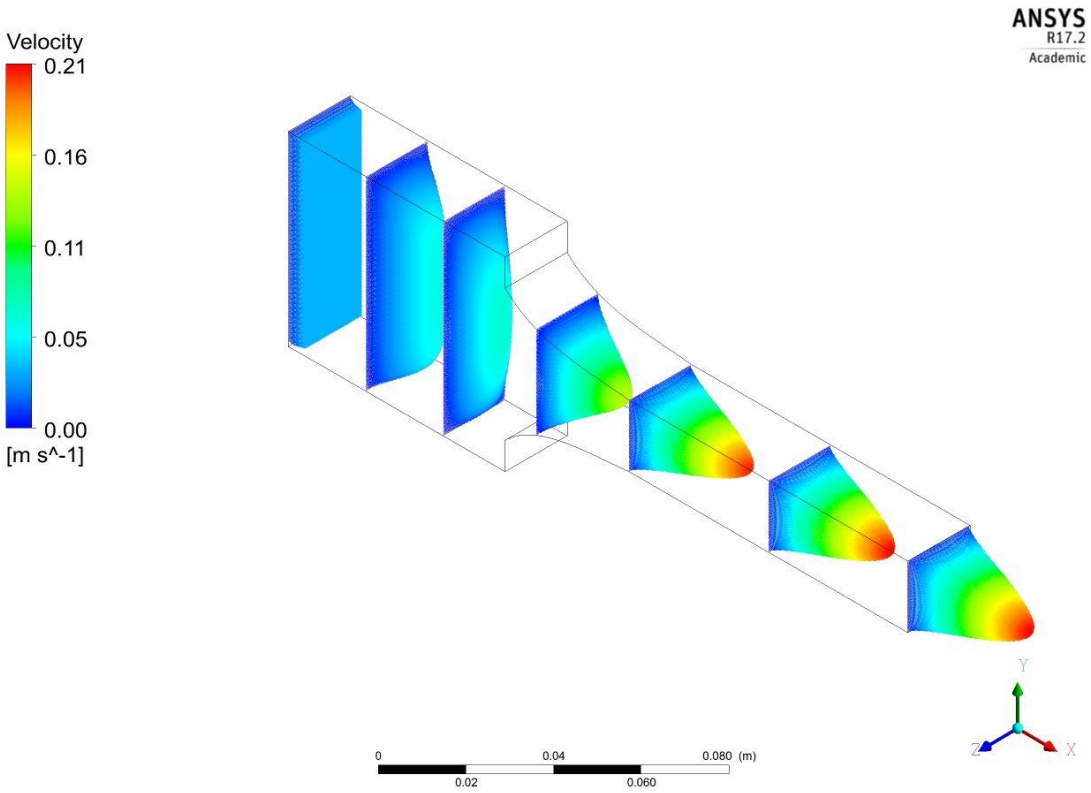

Figure 4.4: Parabolic velocity profiles along different sections of the fluid flow

4.2.2 Velocity gradient along the centerline

At the center of the channel, the flow velocity is the maximum and is assumed to have a parabolic profile along both Y and Z directions. The centerline is depicted in Figure 4.5.

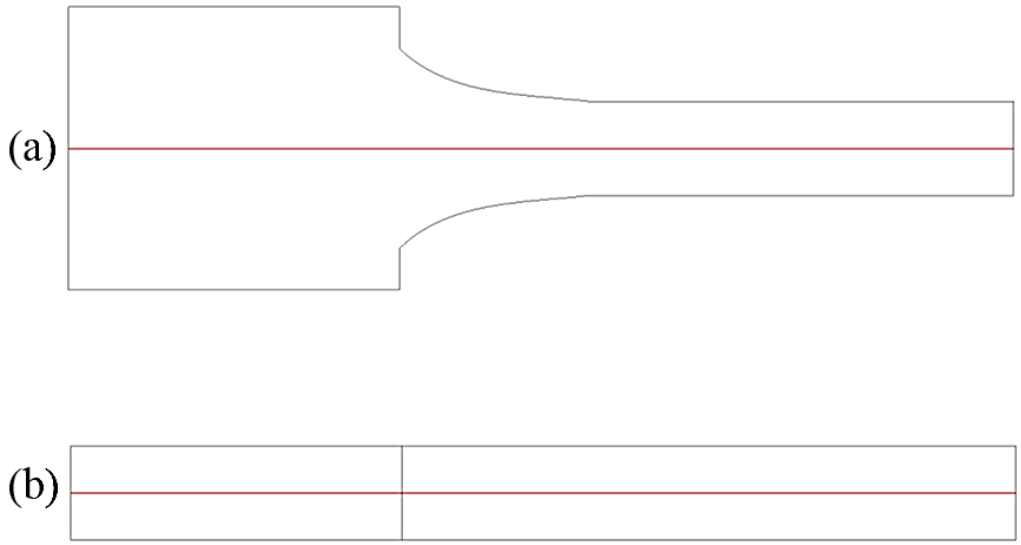

Figure 4.5: Centerline of the channel depicted in red (a) front view and (b) side view

The flow develops in the straight channel and converges in the hyperbolic section. There is an increase in velocity across the convergence. Along the centerline of the system, close examination of the velocity components show dominance by the component along the streamwise direction (x). A plot of the variation of this component vs the position along the channel is shown in Figure 4.6.

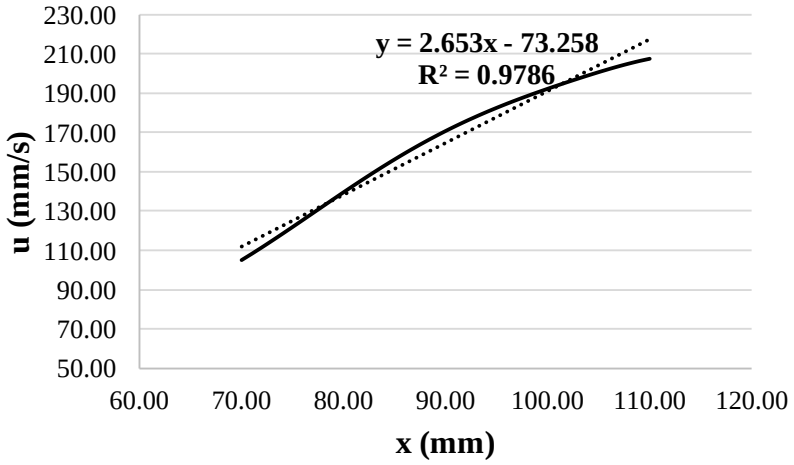

Figure 4.6: Variation of u component of velocity along the centerline (solid curve) and the linear fit (dashed line)

The *x* coordinate shows the position along the channel which spans from 70 mm to 110 mm. The variation in velocity is relatively linear. Taking the derivative with respect to *x* will result in the velocity gradient along this direction.

$$u = 2.653x - 73.258 \tag{4.1}$$

$$\frac{\partial u}{\partial x} = 2.653 \tag{4.2}$$

This is the average extensional rate along this line for the given flow whose magnitude can be used to calculate a Capillary number associated with the droplet. This extensional rate, although has slight deviations, can be assumed to remain fairly constant along the line.

A grid independence study was performed by reducing the number of elements. The results are given in the Table 4.1.

Table 4.1: Grid independence study

Number of elements	Velocity gradient (s^{-1})
129,360	2.63
56,610	2.59

Further simulations were performed using 129,360 elements since it was an acceptable level of accuracy with gain in computational time.

4.2.3 Second invariant of Rate of Deformation tensor

At any given offset position in the *z* direction, the fluid flow behavior is different than along the centerline. This is because of the narrow width of the channel which imposes a strong shear effect on the flow. This effect, combined with the extensional effect imposed by virtue of the hyperbolic contraction, causes the droplets deployed

to behave differently. Figure 4.7 shows the different offset distances where each droplet is injected.

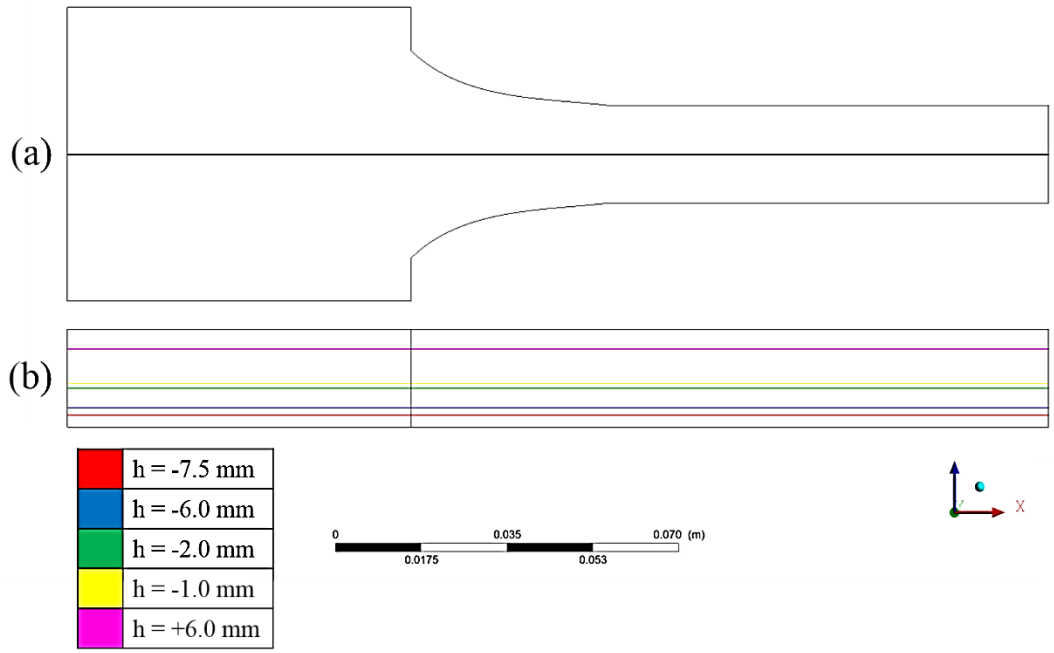

Figure 4.7: Offset deployment positions indicated along (a) centerline in the front view (black) (b) offset distances and color codes

The development and tabulation of the nine components of the velocity gradients are shown in the Appendix B. At positions closer to the wall (z = -10 mm and z = +10 mm), there is a strong influence of *du/dz* which is an order of magnitude higher than *du/dx*. In such cases, the strain rate is calculated as the second invariant of the rate of deformation tensor. The rate of deformation tensor is given by

$$\bar{\bar{D}} = \left(\frac{\partial u_j}{\partial x_i} + \frac{\partial u_i}{\partial x_j}\right) \tag{4.3}$$

From the nine components of the velocity gradient, the second invariant of the rate of deformation tensor can be calculated as

$$S^2 = \left[\frac{\partial u}{\partial x}\left(\frac{\partial u}{\partial x}+\frac{\partial u}{\partial x}\right)+\frac{\partial u}{\partial y}\left(\frac{\partial u}{\partial y}+\frac{\partial v}{\partial x}\right)+\frac{\partial u}{\partial z}\left(\frac{\partial u}{\partial z}+\frac{\partial w}{\partial x}\right)\right]$$
$$+\left[\frac{\partial v}{\partial x}\left(\frac{\partial v}{\partial x}+\frac{\partial u}{\partial y}\right)+\frac{\partial v}{\partial y}\left(\frac{\partial v}{\partial y}+\frac{\partial v}{\partial y}\right)+\frac{\partial v}{\partial z}\left(\frac{\partial v}{\partial z}+\frac{\partial w}{\partial y}\right)\right] \quad (4.4)$$
$$+\left[\frac{\partial w}{\partial x}\left(\frac{\partial w}{\partial x}+\frac{\partial u}{\partial z}\right)+\frac{\partial w}{\partial y}\left(\frac{\partial w}{\partial y}+\frac{\partial v}{\partial z}\right)+\frac{\partial w}{\partial z}\left(\frac{\partial w}{\partial z}+\frac{\partial w}{\partial z}\right)\right]$$

Since the nine components vary in magnitude along each point on the offset lines indicated in Figure 4.7, calculation of the second invariant needs to be performed at each of the chosen points. This provides a framework for calculation of Capillary number of the droplet when it stretches at different points in the channel. The simulation data can be used to calculate the Capillary number to observe the trends.

In the experimental study, the images were obtained and the location of each stretched droplet was determined using MATLAB. The second invariant of the rate of deformation tensor was calculated at the location of the leading end of the droplet. This value was taken and substituted in Equation 1.1 to calculate the Capillary number at the particular position in the channel.

4.3 Summary

Moving closer to the walls, which are at z = -10 mm and z = +10 mm, cause a retardation in the flow because of the no slip boundary condition. However, the shear rate (*du/dz*) increases in magnitude moving closer to the well. Since all the drops are injected along the streamline in the center of the channel, a complete development of all the nine components of the velocity gradients is essential to calculate the magnitude of the strain rate. These nine components along every point on the centerline, for different planes, are shown in Appendix B.

There is a vast difference in magnitude of extensional rate along center and offset streamlines. So, in order to calculate the Capillary number at different points along the channel, data from the velocity gradient tables (in Appendix B) must be referred to get a measure of the strain rate at any specified point in the channel.

Chapter 5: Results and Discussion

Results from the experimental trails are explained in this chapter. The designed flow channel imposes an extensional deformation on the injected droplets. An extensional flow can produce droplets of much smaller size, for a given viscosity ratio, than a shear flow. This means that an extensional flow has more "strength" than a shear flow. Theoretical calculations for droplet breakup in a shear flow has been initially explained in order to validate the concept that it is infeasible to implement. This is followed by the results from running the designed experiments in an extensional flow.

5.1 Droplet Breakup in Shear Flow

For droplets with initial Capillary numbers much higher than the critical Capillary number for a shear flow, calculations were done to determine the length of die required to achieve a certain degree of droplet deformation. The critical capillary number for shear flow is around 0.4 for two immiscible liquids with viscosity ratio of one. Initially, a straight die was envisioned so that droplet breakup could occur in a simple shear flow. In simple shear, the average shear rate is given by Equation 5.1.

$$\dot{\gamma} = \frac{V}{h} \tag{5.1}$$

Where 'V' is the velocity and 'h' is the width of the channel. The width of the die was assumed to be 4 mm and assuming a viscosity ratio of 0.6, Marks' [9] non-dimensional time, from Figure 6, which is shear rate times the actual time, has a value of 12 for the onset of the first bulb in the breakup process. Marks [9] found that in the shear breakup process, the droplet elongates continuously and when the width hits a lower limit, bulbs appear on the end which separate from the main thread. So, for

different velocities of the channel, the shear rates and the corresponding bulb onset times were calculated. The velocity of flow multiplied by the time for bulb onset gave the length of the die needed to produce that deformation and is shown in Table 5.1. This data is valid for droplets of any given capillary number higher than the critical capillary number.

Table 5.1: Die length required to observe bulbs at the ends of a droplet when imposed by shear deformation

Velocity of flow ($mm.s^{-1}$)	**Shear rate in die (s^{-1})**	**Bulb onset time in die (s)**	**Minimum length of die required (mm)**
2	0.5	24	48
4	1.0	12	48
6	1.5	8	48
8	2.0	6	48

From the table, it can be clearly seen that the minimum length of the die needed is around 48 mm. For a die that has a width of 4 mm, it causes the aspect ratio of the die to be around 12:1 which can be very impractical and hard to manufacture. Simple shear was thus not found to be an ideal candidate because it necessitates the usage of long dies which are impractical when potential applications like polymer based additive manufacturing is envisioned. Thus, converging dies were explored which impose extensional deformation on the droplet whose magnitudes are much higher than in shear flow.

5.2 Droplet Deformation in Hyperbolic Channel – Center Deployment

Simulations were performed for the whole range of inlet velocities as per Table 3.2 and the simulation scheme has been explained in Chapter 4. The variation of the velocity in the streamwise direction along the centerline was found and these values are shown in Table 5.2.

Table 5.2: Velocity gradient along the centerline for different inlet speeds

Speed (mm/s)	**U(x)**	**du/dx**
34.08	2.63 *x* - 72.64	2.63
42.02	3.24 *x* - 88.20	3.24
49.96	3.82 *x* - 107.51	3.82
57.90	4.53 *x* - 129.31	4.53
65.84	5.16 *x* - 149.01	5.16
73.78	5.80 *x* - 169.44	5.80

The R^2 value for the linear fit was around 0.98 for all the trials and the slope of the line (*du/dx*) gives the constant extensional rate.

Experiments were performed at the mentioned speeds by introducing a droplet at the central streamline. A series of high speed images were taken and the subject to post processing to figure out the dimensions. Figure 5.1 shows a sample set of images as the droplet flows down the channel.

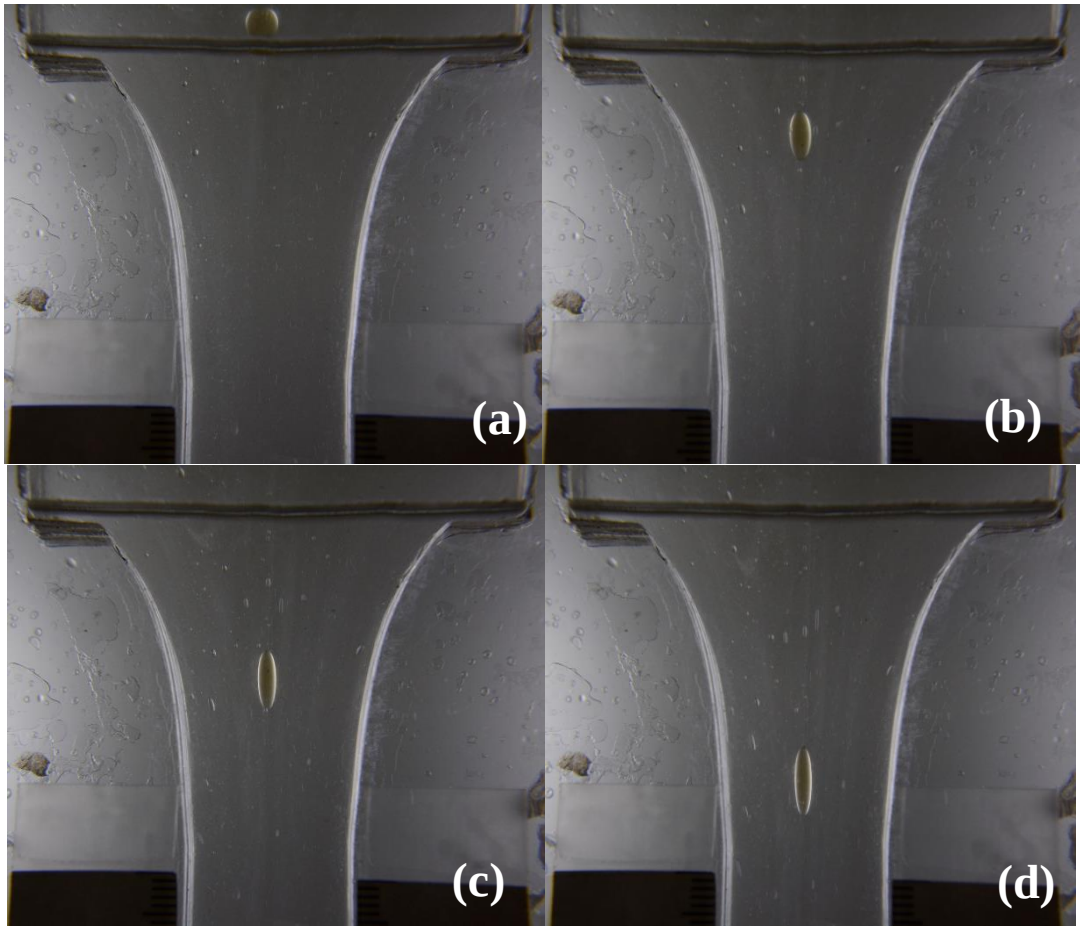

Figure 5.1: Series of images depicting droplet deformation when injected at the center of the channel (a) initial drop before entry into channel (b), (c) and (d) show three frames captured as the droplet travels along the channel

Since the extensional rate along the central streamline is known, the Capillary number associated with the droplet can be easily found for each image. The initial Capillary numbers were calculated and are shown in Table 5.3.

Table 5.3: Initial Capillary number for different experiments

Trial number	Speed (mm/s)	du/dx	Initial Capillary number
1	34.08	2.63	1.97
2	42.02	3.24	2.17
3	49.96	3.82	2.54
4	57.90	4.53	2.87
5	65.84	5.16	3.15
6	73.78	5.80	3.73

From the series of high speed images, the droplet widths were measured at equidistant points in the channel which was then related to the Capillary number. A plot of Capillary number vs. position along the channel as the droplet travelled is shown in Figure 5.2. A linear least squares fit was performed on the data.

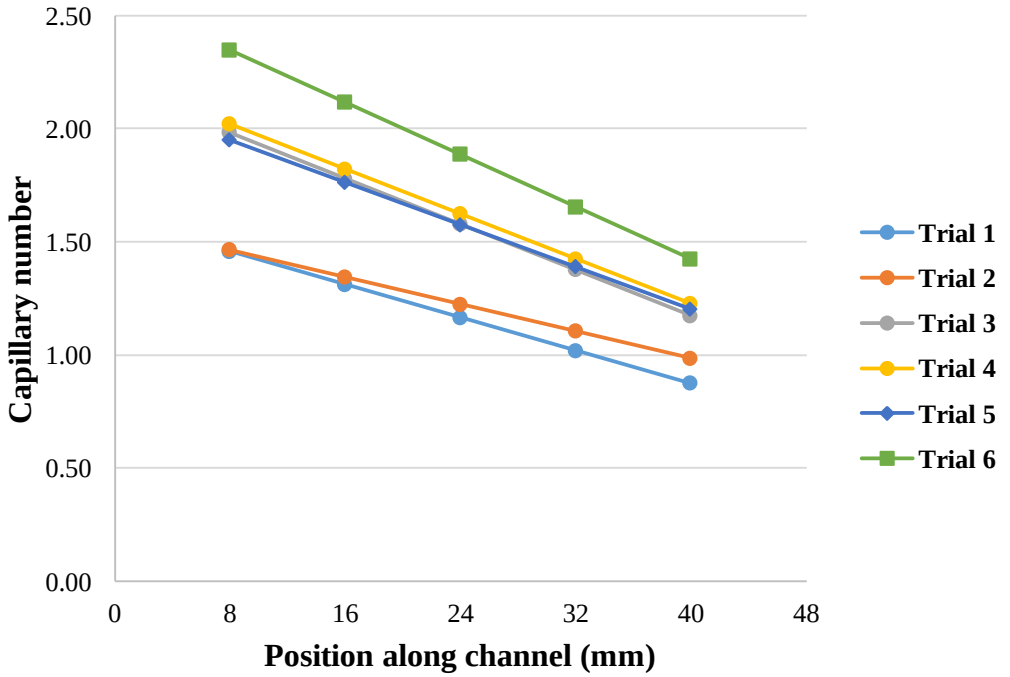

Figure 5.2: Capillary number of the droplet at different positions in the converging channel

Within the experimental error, it was observed that droplets with a higher initial capillary number experience a steeper drop than lower initial capillary numbers. This was corroborated by observations from the plot of normalized droplet length vs. position along the channel at the same locations. Droplet lengths are normalized with initial droplet diameter (*a*). This is depicted in Figure 5.3.

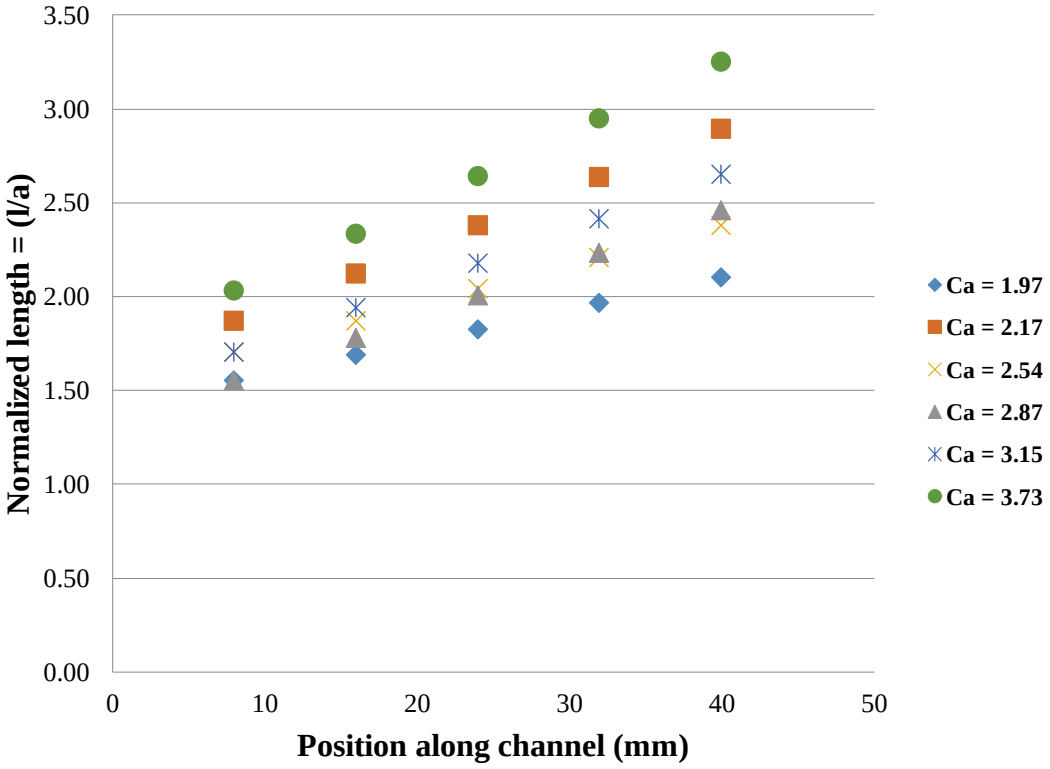

Figure 5.3: Normalized droplet length at different positions in the converging channel

It can be seen from the plot that droplets with higher capillary numbers elongate at a faster rate than lower capillary number droplets. Marks [9] reported that two different sized droplets exposed to the same shear rate (and thus, different capillary numbers) reach the deformed state at the same time. This means that higher capillary numbers must deform at a faster rate and this is clearly evident from the plot and is valid for extensional flow as well.

It is also evident from the figure that the affine state was not reached when the droplet was in the channel. One of the test cases was chosen and the droplet morphology was plotted at equidistant intervals in time from the beginning of the converging channel as it underwent deformation. This was done in order to identify critical changes in morphology at different positions in the channel. Further, it was a check to see if any hint of asymmetry is seen in droplet profile. This plot of droplet width and length is shown in Figure 5.4.

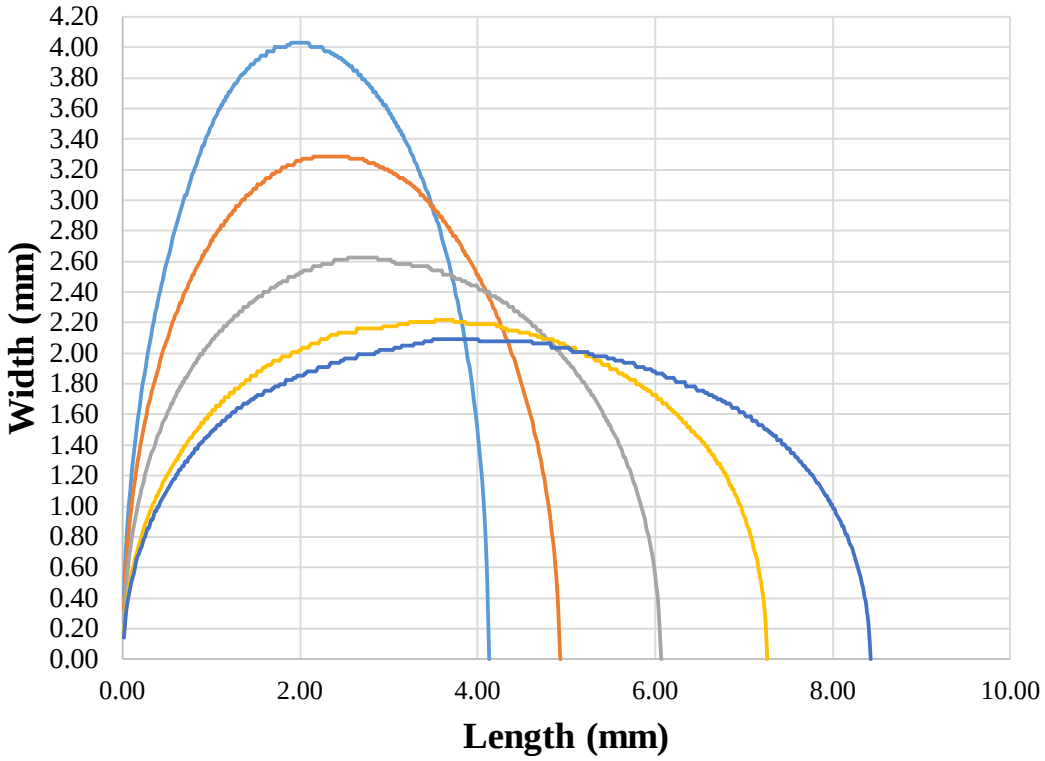

Figure 5.4: Droplet profile at different positions in the converging channel for center deployment (initial Capillary number = 2.54)

The profile at each chosen point in the channel is symmetric and there is neither any evidence of asymmetry due to the converging flow nor there is the observation of affine deformation. The droplet width seems to reduce and reach an asymptote with further reduction requiring the droplet to be present in the converging channel for a

longer duration. Evidently, it seems that there is a limit to the deformation that can be achieved along the central streamline for the designed apparatus. Hence, different points in the channel were investigated to see the effect of the varying extensional rate on the droplet.

5.3 Droplet Deformation in Hyperbolic Channel – Offset Deployment

In the second set of experiments, droplets were injected at different positions in the channel as per Table 3.3. At these positions, there is a combined effect of shear and extension on the droplet. Simulations were performed for the given inlet speed of 34 mm/s and the nine velocity gradients as well as the variation in velocity along each streamline were tabulated. The complete tables are given in the Appendix B. The formula suggested by Mulligan and Rothstein [21] in Equation 3.1 is not applicable since the droplets were no longer along the centerline.

A sample set of images from one of the experiment is shown in Figure 5.5. Evidently, the droplet experienced a different deformation rate than what it observed when deployed in the center of the channel. This is attributed to the large magnitude of the velocity gradient (*du/dz*). Since the width of the channel into the plane is just 20 mm, for the flow condition, large gradients in velocity can be developed. The extensional rate (*du/dx*) still remains fairly constant but the shear effect of *du/dz* imposes a large degree of deformation. The magnitude of *du/dz* is also higher than the extensional rate at the center of the channel from the previous sets of experiments by an order of magnitude. This helps to explain why droplets injected at the center of the channel did not see high degrees of deformations.

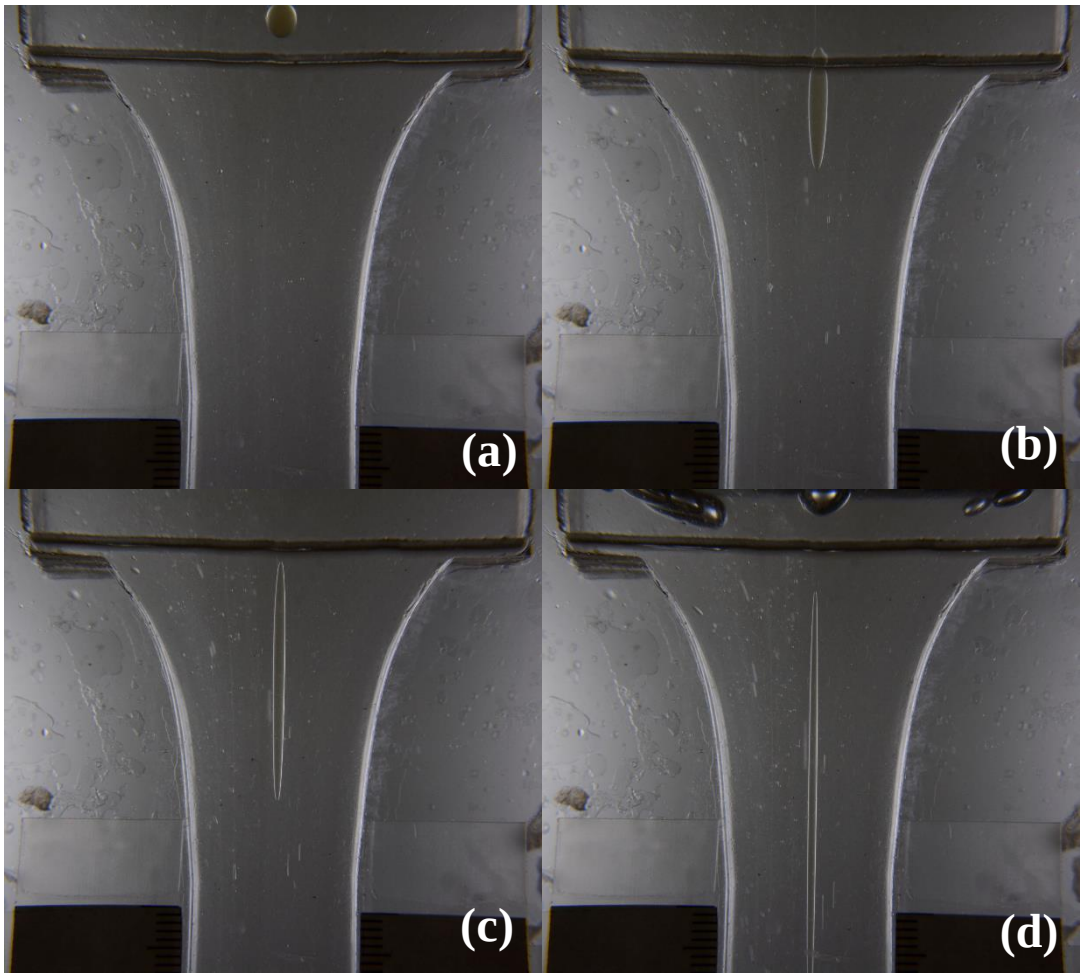

Figure 5.5: Series of images depicting droplet deformation when injected at an offset position in the channel (a) initial drop before entry into channel (b), (c) and (d) show three frames captured as the droplet travels along the channel

For each of the test cases, the trends in droplet profile is shown from Figure 5.6 to Figure 5.10. The measurement method is similar to the scheme used in center deployment tests.

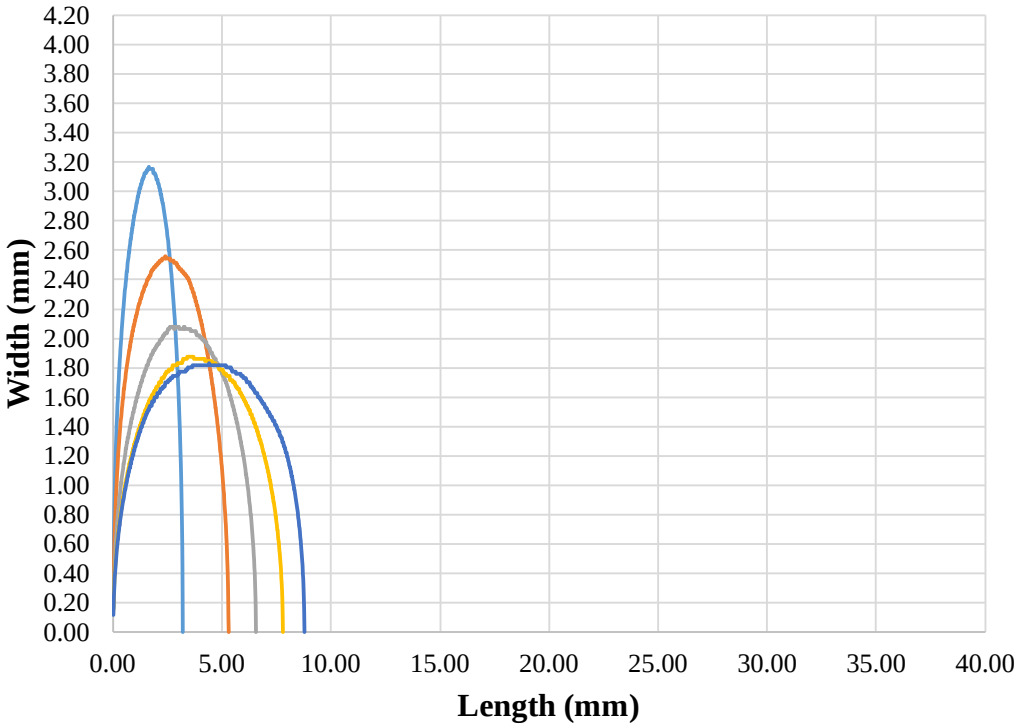

Figure 5.6: Change in droplet morphology for h = -1.0 mm (initial Ca = 2.84)

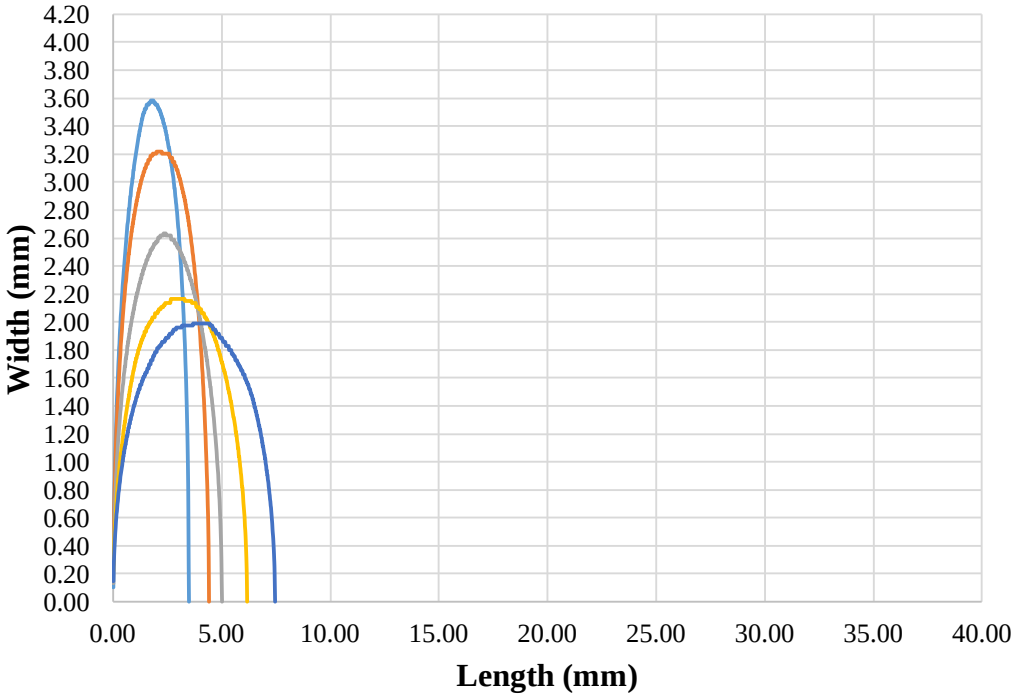

Figure 5.7: Change in droplet morphology for h = -2.0 mm (initial Ca = 4.14)

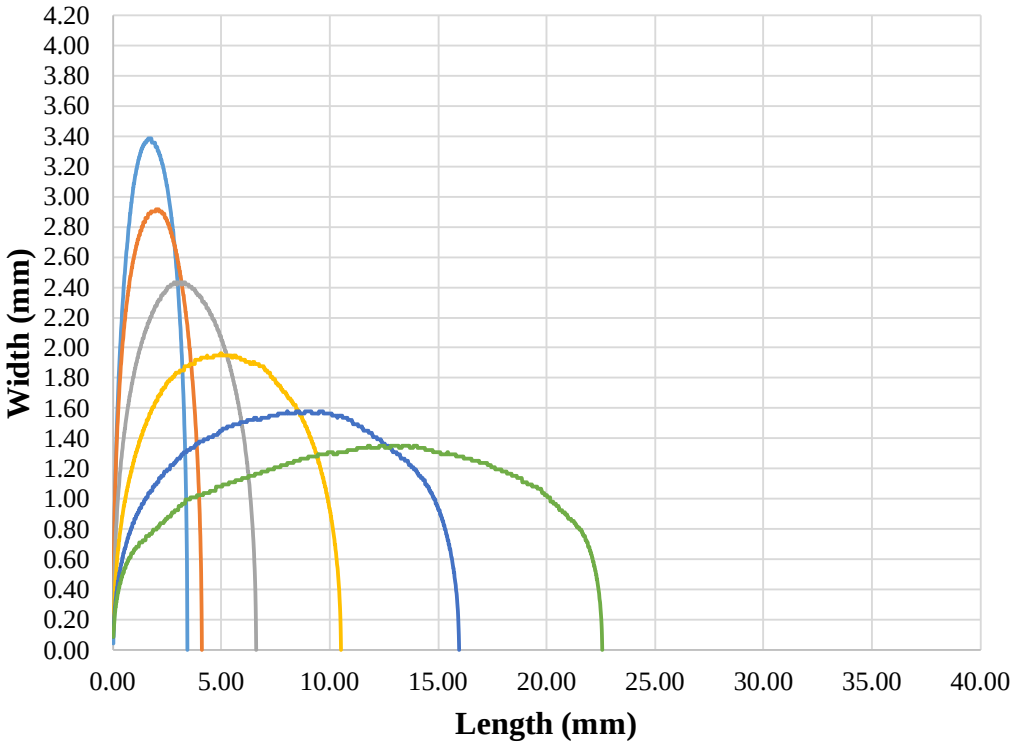

Figure 5.8: Change in droplet morphology for h = -6.0 mm (initial Ca = 9.30)

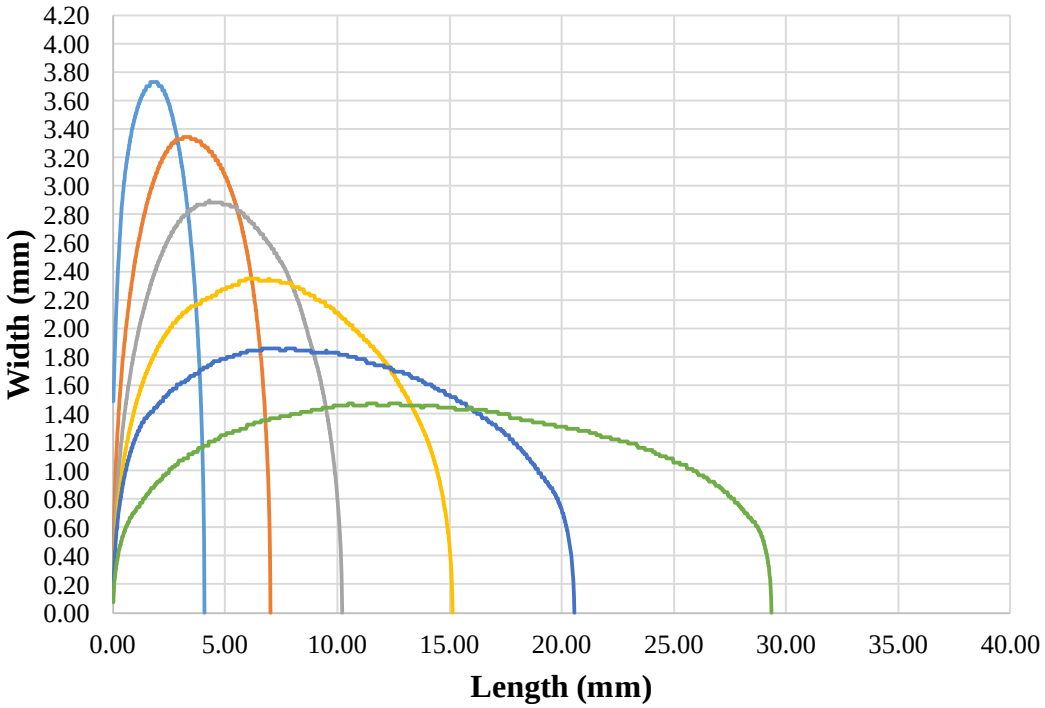

Figure 5.9: Change in droplet morphology for h = +6.0 mm (initial Ca = 10.55)

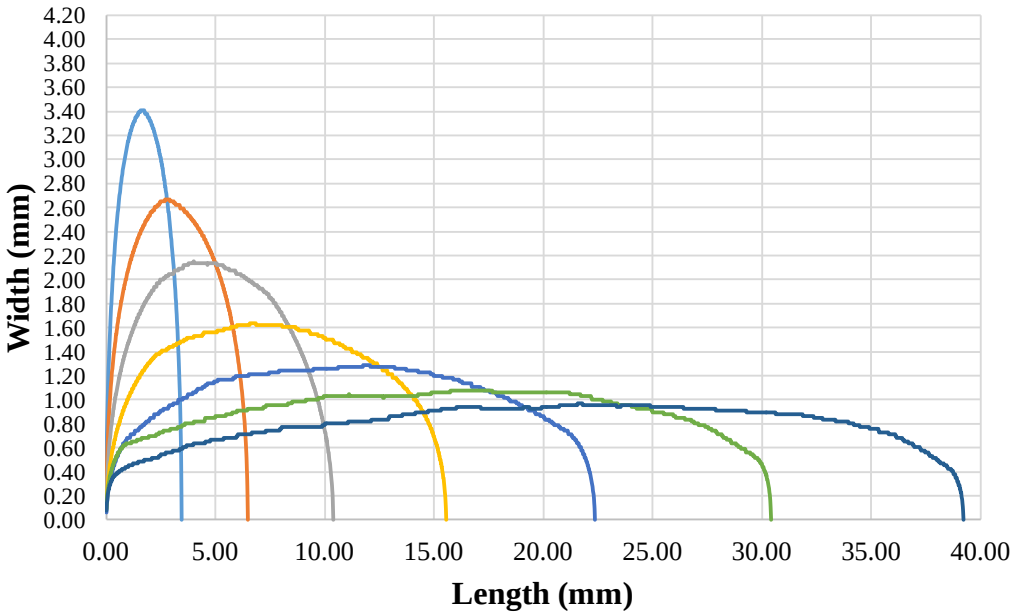

Figure 5.10: Change in droplet morphology for h = -7.5 mm (initial Ca = 11.96)

Droplets closer to the wall edge were stretched more than the droplets closer to the center. Simulation data confirms this where the magnitude of *du/dz* is higher when one moves closer to the wall. It can also be observed from the images that there is a transition of the droplet profile from symmetry to asymmetry as it deforms. Width of the droplet at the center also seems to reach an asymptote for these experiments as well. At the edges of the droplets, especially at droplets injected closer to the wall, the droplet width reduces by a large magnitude over a small length.

The initial Capillary number as well as changes in Capillary number as the droplet moves down the channel is shown in Figure 5.11. The numbers are higher than compared to the central deployment experiments since the extensional rate is higher by an order of magnitude which makes the Capillary number to be very high. Another observation from these experiments is that the stretched droplet is no longer along a straight line drawn from the inlet to the outlet. This phenomenon is depicted in the

Figure 5.12. In a shear flow having a large magnitude of the shear rate, droplets get reoriented from the initial direction and tend to orient themselves along the velocity gradient. This effect was observed in the experiments as well.

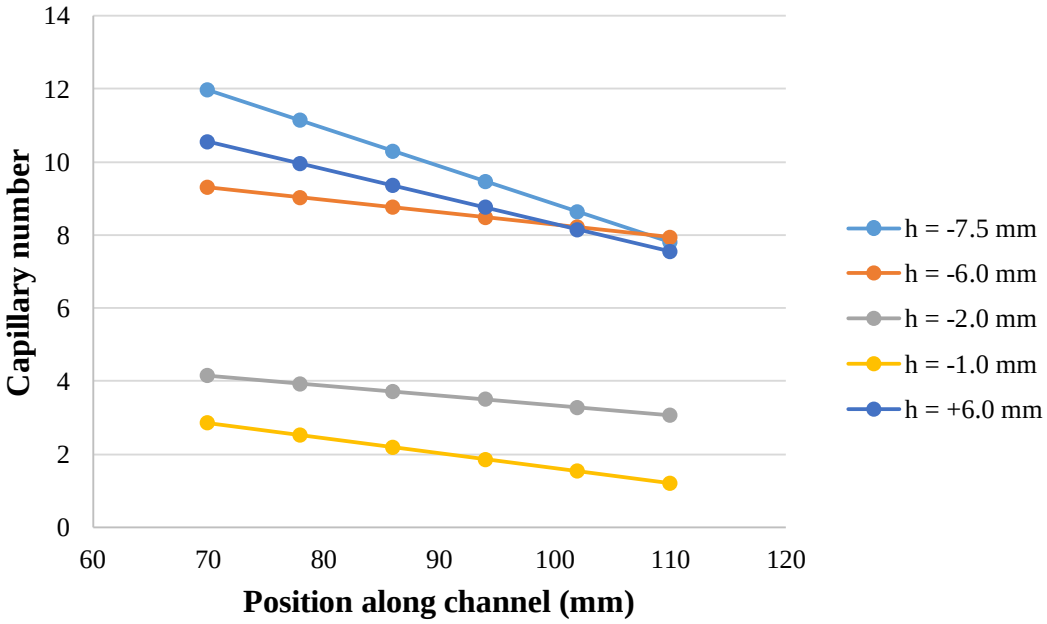

Figure 5.11: Change in Capillary number of droplets injected at different offset distances

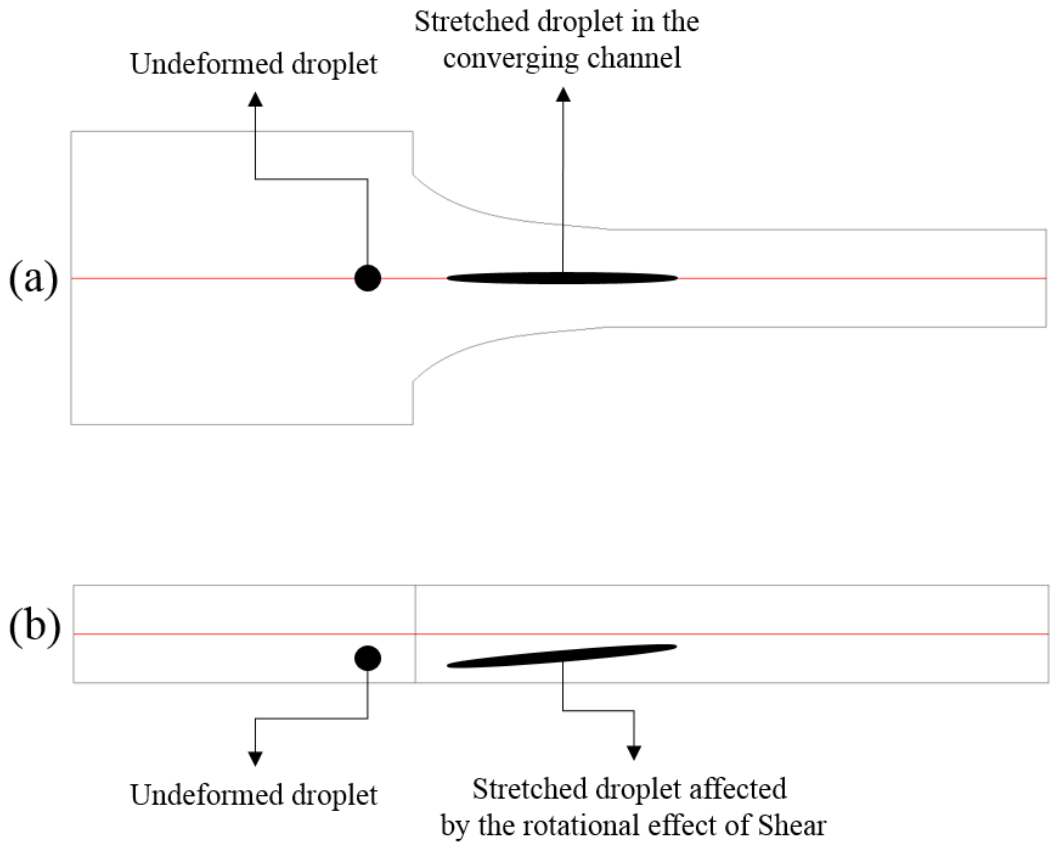

Figure 5.12: Schematic of droplet behavior in offset positions affected by rotationality of Shear

Closer examination of Figure 5.6 to Figure 5.10 indicate that they deviate from a symmetrical profile. Further, there is a rapid reduction in width at the ends of the drops and this width reduces at a slower rate than the width at the center. These points are indicated in Figure 5.13 and Figure 5.14 for two of the test cases.

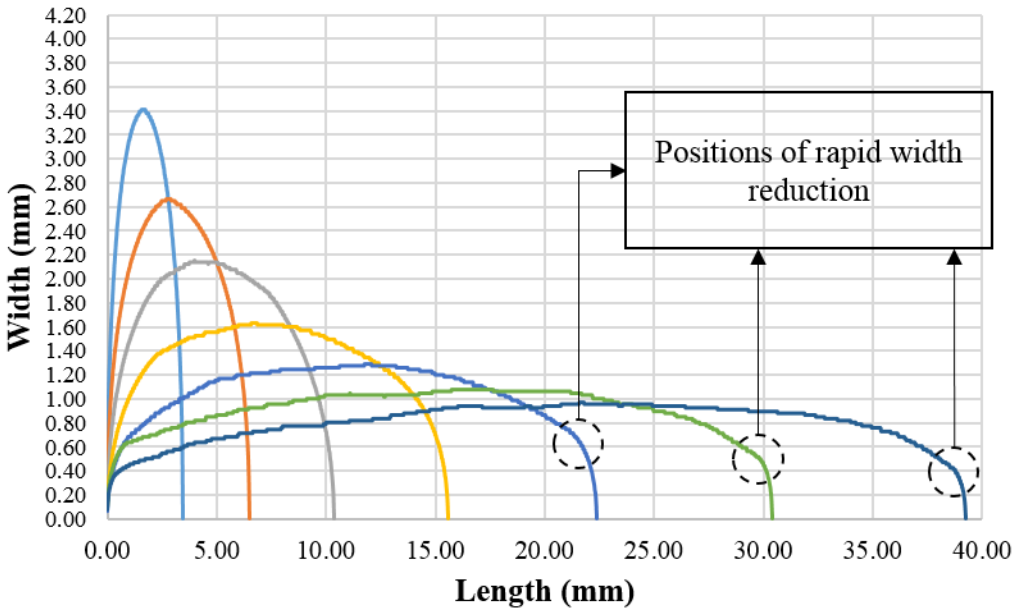

Figure 5.13: Identification of rapid width reduction positions on various droplet profiles for h = -7.5 mm

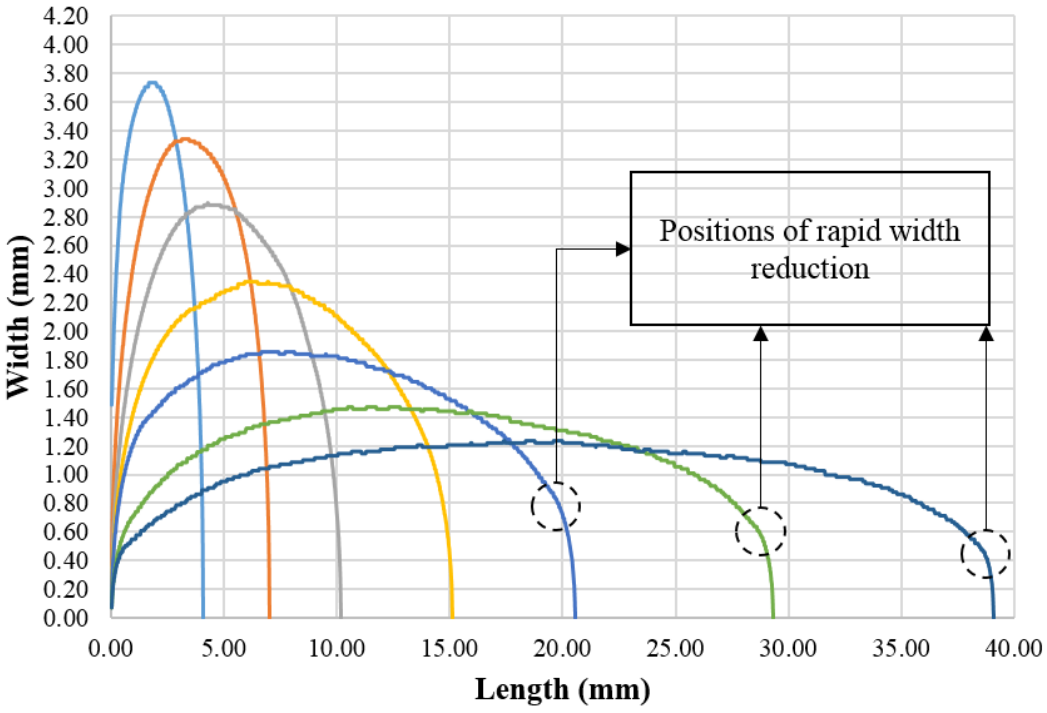

Figure 5.14: Identification of rapid width reduction positions on various droplet profiles for h = +6.0 mm

The Capillary number at these positions are lower than the Capillary number calculated with respect to the width at the center of the droplet. The comparison is indicated in Table 5.4. Further, these points are only discernible when the droplets are deployed closer to the wall, indicating that it is by virtue of the strong shear effect.

Table 5.4: Capillary number comparison using width at the center and width at the leading end

Droplet offset position	**Capillary number based on width at center**	**Capillary number based on width at leading end**
h = -7.5 mm	8.89	4.62
	8.28	3.57
	7.87	3.15
h = +6.0 mm	9.10	4.00
	8.23	3.12
	8.04	2.50

The deformation phenomenon can be theorized as follows. The droplet stretches and reaches a state where its width near the leading and trailing end reaches a constant value while the width at the center is still reducing. The conical shape at the ends is quite evident from the images in Figure 5.5 and it can be assumed that the diameter of the base of the cone remains constant at which stage, the remaining volume is shed from the width of the droplet at the center to aid extension.

If the droplet is in the hyperbolic field for a longer period, it will reach a stage where the width at the center becomes equal to the width near the leading and trailing end. This is the stage where the external field renders the droplet to be unsteady, causing eventual breakup.

5.4 Summary

While estimating the strength of different kinds of flows to impart a degree of deformation on a droplet suspended in the field, it was found that a shear flow was ineffective to deform the droplet compared to an extensional flow. The apparatus designed to impose a constant extensional rate on a droplet injected at the center of the field resulted in different droplet behaviors on different streamlines. Simulation results showed that the extensional rate remained fairly constant along the central streamline but there was a strong influence of a shear component along other streamlines.

The results from the experiments performed on droplet deformation in a hyperbolic field illuminated interesting insights into the process. No droplet reached the affine state when deployed in the center of the channel while a higher degree of deformation was seen when injected in the offset position. The strength of the field was able to reduce the Capillary number to a certain degree which revealed the dynamics behind the deformation of a droplet.

Droplets that started with a higher initial Capillary number attained width reduction at a faster rate than droplets with lower initial Capillary number. This fact was true for both center deployment as well as offset deployment experiments. The analysis of the attainment of the affine state revealed that the droplets attained a near constant width at the leading and trailing ends which had a lower Capillary number than the Capillary number measured with respect to the center. Further experiments are

necessary to analyze the behavior along different streamlines as well as devising different versions of the hyperbolic channel which have stronger contractions.

Chapter 6: Conclusion and Future Studies

This research worked aimed to understand the fundamental phenomenon of immiscible droplet behavior in a flow field. Most of the research in this area has been performed using laboratory equipment like a four-roll mill which does not have any practical applicability. This motivated the development of a practical die that can impose a certain degree of deformation on an immiscible droplet. In specific, this research looked into the behavior of a droplet in a definable flow field which can be developed in a hyperbolic die.

The study explored droplet deformation, filament formation and filament breakup in a fundamental extensional flow. An apparatus was designed and built to study the deformation induced on an immiscible droplet of Castor oil by a flow field of Silicone oil. The flow channel had a hyperbolic profile which has the property of imposing a constant extensional rate on a droplet placed at the center of the channel. A constant extensional rate allows easy modelling of the process and eliminates it as a parameter. The simulation results confirmed the extensional rate being constant across the center as well as the existence of a strong shear effect in the offset planes. Droplets were injected at different positions in the channel to observe how they stretched in the flow field. Many insights were revealed into the dynamics of droplet deformation such as non-attainment of the affine state on droplets injected into the center and rapid stretch and pointed ends of the droplet injected at different planes. Combined shear and extensional effect need to be taken into account at droplets injected into the offset position.

Although the extensional rate can be assumed to be constant across the converging channel, there is a variation of about 2% from a constant value. However, some researchers have shown that reducing the depth of the channel into the plane, leading to a Hele-Shaw like flow, can make the extensional rate more uniform along the channel. Theoretical development, assuming 2D approximations, using lubrication theory needs to be done to reveal the fundamental aspects at play. Further, the effect of the pressure driven flow need to be taken into account since the current system uses a plunger to impose a velocity. The difference in pressure between the leading and trailing ends can affect the dynamics of droplet deformation.

Since the channel used in the experiment was unable to stretch the droplets injected into the center, newer versions of the channel have to be designed that have stronger convergences which may lead to attainment of the affine state in the center of the channel itself. This deformation can be compared to the affine deformation seen by injection into the offset position on the current apparatus. Finally, the camera and imaging setup can be improved with proper illumination on the droplet. The image acquisition and processing system needs to be made more robust to capture minute details on the deforming droplet.

Appendix A – Image processing code

```
close all;

clear all;

clc;



source='?-??-???.png';              % This is the source generic image



date='211';                         % Date with MDD as format

trial=8;                            % Trial number

num=8;                              % Number of images in the trial folder



imagewidth=5472;                    % Image size properties in pixel units

imageheight=3080;

% The information entered is inserted into the generic source file

source(1)=date(1);

source(3)=date(2);

source(4)=date(3);

source(6)=string(trial);

% Empty arrays are created to denote drop properties, which will be added

Transcient_Area=[];

Transcient_Aspect=[];

Transcient_Center=[];

Transcient_Box=[];
```

```
width=[];



for j=0:num

    if j<10

        source(7)=string(0);

        source(8)=string(j);

    elseif j>=10

        source(7)=string(1);

        source(8)=string(j-10);

    end

    file=imread(source);

    file=rgb2gray(file);            % Image converted to grayscale

    file=im2bw(file);               % Image converted to binary

    file=imcomplement(file);        % Image is inverted

    figure(1);

    imshow(file);                   % Shows resulting image



    data=bwconncomp(file, 4)        % Finds connected components in image

    data.NumObjects

    data=regionprops(data,'Area','Centroid','BoundingBox','Eccentricity')

    % Measures properties of connected components

    ecc=[data.Eccentricity];

    areas=[data.Area];

    centers=[data.Centroid];
```

```
    box=[data.BoundingBox];
    aspect_ratio=(1-ecc.^2).^(-0.5);


    [a,n]=max(areas);               % Finds components with maximum area
    drop_area=areas(n);
    drop_aspect=aspect_ratio(n);
    drop_center=[centers(2*n-1),centers(2*n)];
    drop_box=[box(4*n-3),box(4*n-2),box(4*n-1),box(4*n)];
% Information is inserted into the empty arrays
    Transcient_Area=[Transcient_Area;drop_area];
    Transcient_Aspect=[Transcient_Aspect;drop_aspect];
    Transcient_Center=[Transcient_Center;drop_center];
    Transcient_Box=[Transcient_Box;drop_box];
    b=[];
    for y=1:imageheight
        count=0;
        for x=1:imagewidth
            color=file(y,x);        % Determines value of pixel and location
            if color>0              % If pixel is white (1), add 1 at count
                count=count+1;
            end
        end
        b=[b;count];
    end
```

```
    width=[width,b];
end
Total=[Transcient_Area,Transcient_Aspect,Transcient_Center,Transcient_Box];
Sections=[width];
file1='?-??-?data.xlsx';            % Generic Excel file for drop data
file1(1)=date(1);                   % Information entered is inserted
file1(3)=date(2);
file1(4)=date(3);
file1(6)=string(trial);
file2='?-??-?sections.xlsx';        % Generic drop section data file
file2(1)=date(1);                   % Information entered is inserted
file2(3)=date(2);
file2(4)=date(3);
file2(6)=string(trial);
xlswrite(file1,Total);              % Creates Excel file for drop data
xlswrite(file2,Sections);           % Creates Excel file for drop section
```

Appendix B – Calculation of the second invariant of the rate of deformation tensor

The following section tabulates the complete development of the nine components of the velocity gradient tensor along different streamlines of the flow field for an inlet velocity of 34 mm/s. The values from the tables were used to calculate the Capillary number associated with different positions along the channel as shown in Chapter 5. The tables only provide data for the velocity gradients in the converging zone (which begins at x = 70 mm) for each offset distance indicated in Table 3.3.

The nine columns in the Tables B.1 to B.5 indicate each component of the velocity gradient. Using these values, the second invariant of the rate of deformation tensor can be calculated which is indicated in the last column.

The second invariant (S^2) can be used in Equation 1.1 to find the Capillary number at any given point along the line.

Table B.1: Second invariant values at each point along h = -1.0 mm

Position along x (mm)	du/dx	du/dy	du/dz	dv/dx	dv/dy	dv/dz	dw/dx	dw/dy	dw/dz	S^2
70.00	3.15	0.00	-1.96	0.00	-3.17	0.00	0.00	0.00	0.04	3.71
70.70	3.20	0.00	-1.99	0.00	-3.24	0.00	0.00	0.00	0.04	3.77
71.42	3.26	0.00	-2.03	0.00	-3.31	0.00	0.00	0.00	0.04	3.84
72.17	3.33	0.00	-2.08	0.00	-3.37	0.00	0.00	0.00	0.04	3.93
72.94	3.38	0.00	-2.12	0.00	-3.42	0.00	0.00	0.00	0.04	3.99
73.73	3.43	0.00	-2.17	0.00	-3.47	0.00	0.00	0.00	0.04	4.06
74.53	3.47	0.00	-2.21	0.00	-3.51	0.00	0.00	0.00	0.04	4.11
75.35	3.50	0.00	-2.26	0.00	-3.54	0.00	0.00	0.00	0.04	4.16
76.19	3.51	0.00	-2.31	0.00	-3.55	0.00	0.00	0.00	0.04	4.20
77.03	3.52	0.00	-2.35	0.00	-3.56	0.00	0.00	0.00	0.04	4.23
77.90	3.52	0.00	-2.40	0.00	-3.56	0.00	0.00	0.00	0.04	4.26
78.78	3.50	0.00	-2.45	0.00	-3.54	0.00	0.00	0.00	0.04	4.28
79.66	3.48	0.00	-2.50	0.00	-3.51	0.00	0.00	0.00	0.04	4.28
80.56	3.44	0.00	-2.55	0.00	-3.48	0.00	0.00	0.00	0.04	4.28
81.46	3.39	0.00	-2.60	0.00	-3.43	0.00	0.00	0.00	0.04	4.27
82.38	3.33	0.00	-2.64	0.00	-3.37	0.00	0.00	0.00	0.04	4.25
83.30	3.26	0.00	-2.69	0.00	-3.30	0.00	0.00	0.00	0.03	4.23
84.22	3.19	0.00	-2.73	0.00	-3.22	0.00	0.00	0.00	0.03	4.19
85.15	3.10	0.00	-2.77	0.00	-3.13	0.00	0.00	0.00	0.03	4.16
86.08	3.01	0.00	-2.81	0.00	-3.04	0.00	0.00	0.00	0.03	4.12
87.03	2.92	0.00	-2.85	0.00	-2.94	0.00	0.00	0.00	0.03	4.08
87.98	2.82	0.00	-2.89	0.00	-2.84	0.00	0.00	0.00	0.03	4.04
88.93	2.71	0.00	-2.93	0.00	-2.74	0.00	0.00	0.00	0.03	4.00
89.87	2.61	0.00	-2.97	0.00	-2.64	0.00	0.00	0.00	0.02	3.96
90.82	2.51	0.00	-3.01	0.00	-2.53	0.00	0.00	0.00	0.02	3.92
91.77	2.41	0.00	-3.04	0.00	-2.43	0.00	0.00	0.00	0.02	3.88
92.72	2.31	0.00	-3.08	0.00	-2.34	0.00	0.00	0.00	0.02	3.85
93.68	2.22	0.00	-3.11	0.00	-2.24	0.00	0.00	0.00	0.02	3.82
94.63	2.13	0.00	-3.14	0.00	-2.16	0.00	0.00	0.00	0.02	3.80
95.58	2.05	0.00	-3.17	0.00	-2.07	0.00	0.00	0.00	0.02	3.78
96.54	1.98	0.00	-3.20	0.00	-2.00	0.00	0.00	0.00	0.02	3.76
97.50	1.91	0.00	-3.22	0.00	-1.93	0.00	0.00	0.00	0.02	3.75
98.47	1.85	0.00	-3.25	0.00	-1.88	0.00	0.00	0.00	0.02	3.74
99.44	1.80	0.00	-3.27	0.00	-1.83	0.00	0.00	0.00	0.02	3.74
100.40	1.76	0.00	-3.29	0.00	-1.78	0.00	0.00	0.00	0.02	3.74
101.37	1.72	0.00	-3.32	0.00	-1.75	0.00	0.00	0.00	0.03	3.74
102.32	1.69	0.00	-3.34	0.00	-1.71	0.00	0.00	0.00	0.03	3.74
103.28	1.65	0.00	-3.36	0.00	-1.68	0.00	0.00	0.00	0.03	3.74
104.23	1.61	0.00	-3.38	0.00	-1.63	0.00	0.00	0.00	0.03	3.74
105.19	1.56	0.00	-3.40	0.00	-1.58	0.00	0.00	0.00	0.02	3.74
106.15	1.49	0.00	-3.41	0.00	-1.52	0.00	0.00	0.00	0.02	3.73
107.11	1.41	0.00	-3.43	0.00	-1.43	0.00	0.00	0.00	0.02	3.71
108.08	1.31	0.00	-3.44	0.00	-1.32	0.00	0.00	0.00	0.01	3.68
109.04	1.18	0.00	-3.44	0.00	-1.19	0.00	0.00	0.00	0.01	3.64
110.00	1.04	0.00	-3.43	0.00	-1.04	0.00	0.00	0.00	0.00	3.58

Table B.2: Second invariant values at each point along h = -2.0 mm

Position along x (mm)	du/dx	du/dy	du/dz	dv/dx	dv/dy	dv/dz	dw/dx	dw/dy	dw/dz	S^2
70.00	3.07	0.00	-3.92	0.00	-3.08	0.00	0.00	0.00	0.03	4.98
70.70	3.12	0.00	-4.00	0.00	-3.16	0.00	0.00	0.00	0.03	5.07
71.42	3.18	0.00	-4.08	0.00	-3.22	0.00	0.00	0.00	0.03	5.17
72.17	3.25	0.00	-4.16	0.00	-3.28	0.00	0.00	0.00	0.03	5.28
72.94	3.30	0.00	-4.25	0.00	-3.33	0.00	0.00	0.00	0.03	5.38
73.73	3.35	0.00	-4.34	0.00	-3.38	0.00	0.00	0.00	0.03	5.48
74.53	3.38	0.00	-4.43	0.00	-3.42	0.00	0.00	0.00	0.03	5.57
75.35	3.41	0.00	-4.52	0.00	-3.44	0.00	0.00	0.00	0.03	5.66
76.19	3.43	0.00	-4.62	0.00	-3.46	0.00	0.00	0.00	0.03	5.75
77.03	3.43	0.00	-4.71	0.00	-3.47	0.00	0.00	0.00	0.03	5.83
77.90	3.43	0.00	-4.81	0.00	-3.46	0.00	0.00	0.00	0.03	5.91
78.78	3.42	0.00	-4.91	0.00	-3.45	0.00	0.00	0.00	0.03	5.99
79.66	3.39	0.00	-5.01	0.00	-3.42	0.00	0.00	0.00	0.03	6.05
80.56	3.36	0.00	-5.11	0.00	-3.39	0.00	0.00	0.00	0.03	6.11
81.46	3.31	0.00	-5.21	0.00	-3.34	0.00	0.00	0.00	0.03	6.17
82.38	3.25	0.00	-5.30	0.00	-3.28	0.00	0.00	0.00	0.03	6.22
83.30	3.19	0.00	-5.40	0.00	-3.21	0.00	0.00	0.00	0.03	6.27
84.22	3.11	0.00	-5.49	0.00	-3.14	0.00	0.00	0.00	0.03	6.31
85.15	3.03	0.00	-5.57	0.00	-3.05	0.00	0.00	0.00	0.02	6.34
86.08	2.94	0.00	-5.66	0.00	-2.96	0.00	0.00	0.00	0.02	6.38
87.03	2.85	0.00	-5.75	0.00	-2.87	0.00	0.00	0.00	0.02	6.41
87.98	2.75	0.00	-5.83	0.00	-2.77	0.00	0.00	0.00	0.02	6.45
88.93	2.65	0.00	-5.91	0.00	-2.67	0.00	0.00	0.00	0.02	6.48
89.87	2.55	0.00	-5.99	0.00	-2.57	0.00	0.00	0.00	0.02	6.51
90.82	2.45	0.00	-6.07	0.00	-2.47	0.00	0.00	0.00	0.02	6.54
91.77	2.36	0.00	-6.14	0.00	-2.37	0.00	0.00	0.00	0.02	6.58
92.72	2.26	0.00	-6.21	0.00	-2.28	0.00	0.00	0.00	0.02	6.61
93.68	2.17	0.00	-6.27	0.00	-2.19	0.00	0.00	0.00	0.02	6.64
94.63	2.09	0.00	-6.33	0.00	-2.10	0.00	0.00	0.00	0.02	6.67
95.58	2.01	0.00	-6.39	0.00	-2.03	0.00	0.00	0.00	0.02	6.70
96.54	1.94	0.00	-6.45	0.00	-1.95	0.00	0.00	0.00	0.02	6.73
97.50	1.87	0.00	-6.50	0.00	-1.89	0.00	0.00	0.00	0.02	6.77
98.47	1.82	0.00	-6.56	0.00	-1.83	0.00	0.00	0.00	0.02	6.80
99.44	1.77	0.00	-6.61	0.00	-1.78	0.00	0.00	0.00	0.02	6.84
100.40	1.72	0.00	-6.65	0.00	-1.74	0.00	0.00	0.00	0.02	6.87
101.37	1.69	0.00	-6.70	0.00	-1.71	0.00	0.00	0.00	0.02	6.91
102.32	1.65	0.00	-6.74	0.00	-1.67	0.00	0.00	0.00	0.02	6.94
103.28	1.62	0.00	-6.79	0.00	-1.64	0.00	0.00	0.00	0.02	6.98
104.23	1.58	0.00	-6.83	0.00	-1.60	0.00	0.00	0.00	0.02	7.01
105.19	1.53	0.00	-6.87	0.00	-1.55	0.00	0.00	0.00	0.02	7.04
106.15	1.46	0.00	-6.91	0.00	-1.48	0.00	-0.01	0.00	0.02	7.06
107.11	1.38	0.00	-6.95	0.00	-1.40	0.00	-0.01	0.00	0.01	7.09
108.08	1.28	0.00	-6.99	0.00	-1.29	0.00	-0.01	0.00	0.01	7.11
109.04	1.16	0.00	-7.03	0.00	-1.16	0.00	-0.01	0.00	0.01	7.13
110.00	1.01	0.00	-7.08	0.00	-1.02	0.00	-0.01	0.00	0.00	7.15

Table B.3: Second invariant values at each point along h = -6.0 mm

Position along x (mm)	du/dx	du/dy	du/dz	dv/dx	dv/dy	dv/dz	dw/dx	dw/dy	dw/dz	S^2
70.00	2.17	0.00	12.39	0.00	-2.13	0.00	0.01	0.00	-0.02	12.58
70.70	2.20	0.00	12.65	0.00	-2.18	0.00	0.00	0.00	-0.02	12.84
71.42	2.24	0.00	12.92	0.00	-2.23	0.00	-0.01	0.00	-0.02	13.11
72.17	2.30	0.00	13.20	0.00	-2.27	0.00	-0.01	0.00	-0.02	13.40
72.94	2.33	0.00	13.50	0.00	-2.31	0.00	0.00	0.00	-0.02	13.70
73.73	2.37	0.00	13.81	0.00	-2.35	0.00	0.00	0.00	-0.02	14.01
74.53	2.39	0.00	14.13	0.00	-2.37	0.00	0.00	0.00	-0.02	14.33
75.35	2.42	0.00	14.46	0.00	-2.39	0.00	0.00	0.00	-0.02	14.66
76.19	2.43	0.00	14.79	0.00	-2.41	0.00	0.00	0.00	-0.02	14.99
77.03	2.44	0.00	15.13	0.00	-2.42	0.00	0.00	0.00	-0.02	15.33
77.90	2.44	0.00	15.48	0.00	-2.42	0.00	0.00	0.00	-0.02	15.67
78.78	2.43	0.00	15.83	0.00	-2.41	0.00	0.00	0.00	-0.02	16.02
79.66	2.41	0.00	16.18	0.00	-2.39	0.00	0.00	0.00	-0.02	16.36
80.56	2.39	0.00	16.54	0.00	-2.37	0.00	0.00	0.00	-0.02	16.71
81.46	2.36	0.00	16.89	0.00	-2.34	0.00	0.00	0.00	-0.02	17.05
82.38	2.32	0.00	17.24	0.00	-2.30	0.00	0.00	0.00	-0.02	17.39
83.30	2.27	0.00	17.58	0.00	-2.26	0.00	0.00	0.00	-0.02	17.73
84.22	2.22	0.00	17.92	0.00	-2.21	0.00	0.00	0.00	-0.02	18.06
85.15	2.17	0.00	18.25	0.00	-2.15	0.00	0.00	0.00	-0.02	18.38
86.08	2.11	0.00	18.57	0.00	-2.09	0.00	0.00	0.00	-0.02	18.69
87.03	2.04	0.00	18.89	0.00	-2.03	0.00	0.00	0.00	-0.02	19.00
87.98	1.97	0.00	19.20	0.00	-1.96	0.00	0.00	0.00	-0.01	19.30
88.93	1.91	0.00	19.49	0.00	-1.89	0.00	0.00	0.00	-0.01	19.58
89.87	1.84	0.00	19.77	0.00	-1.82	0.00	0.00	0.00	-0.01	19.86
90.82	1.77	0.00	20.05	0.00	-1.75	0.00	0.00	0.00	-0.01	20.12
91.77	1.70	0.00	20.31	0.00	-1.69	0.00	0.00	0.00	-0.01	20.38
92.72	1.63	0.00	20.56	0.00	-1.62	0.00	0.00	0.00	-0.01	20.63
93.68	1.57	0.00	20.80	0.00	-1.56	0.00	0.00	0.00	-0.01	20.86
94.63	1.52	0.00	21.03	0.00	-1.50	0.00	0.00	0.00	-0.01	21.09
95.58	1.46	0.00	21.25	0.00	-1.45	0.00	0.00	0.00	-0.01	21.30
96.54	1.41	0.00	21.47	0.00	-1.40	0.00	0.00	0.00	-0.01	21.52
97.50	1.37	0.00	21.68	0.00	-1.36	0.00	0.00	0.00	-0.01	21.72
98.47	1.33	0.00	21.88	0.00	-1.32	0.00	0.00	0.00	-0.01	21.92
99.44	1.30	0.00	22.07	0.00	-1.29	0.00	0.00	0.00	-0.01	22.11
100.40	1.28	0.00	22.26	0.00	-1.26	0.00	0.00	0.00	-0.01	22.29
101.37	1.25	0.00	22.44	0.00	-1.24	0.00	0.00	0.00	-0.01	22.47
102.32	1.23	0.00	22.61	0.00	-1.21	0.00	0.00	0.00	-0.02	22.65
103.28	1.21	0.00	22.78	0.00	-1.19	0.00	0.00	0.00	-0.02	22.82
104.23	1.18	0.00	22.95	0.00	-1.16	0.00	0.00	0.00	-0.01	22.98
105.19	1.14	0.00	23.11	0.00	-1.12	0.00	0.00	0.00	-0.01	23.14
106.15	1.09	0.00	23.27	0.00	-1.07	0.00	0.01	0.00	-0.01	23.30
107.11	1.02	0.00	23.42	0.00	-1.01	0.00	0.01	0.00	-0.01	23.44
108.08	0.94	0.00	23.56	0.00	-0.93	0.00	0.01	0.00	-0.01	23.58
109.04	0.84	0.00	23.70	0.00	-0.83	0.00	0.01	0.00	-0.01	23.71
110.00	0.73	0.00	23.81	0.00	-0.72	0.00	0.01	0.00	0.00	23.83

Table B.4: Second invariant values at each point along h = +6.0 mm

Position along x (mm)	du/dx	du/dy	du/dz	dv/dx	dv/dy	dv/dz	dw/dx	dw/dy	dw/dz	S^2
70.00	2.17	0.00	-12.39	0.00	-2.13	0.00	-0.01	0.00	-0.02	12.58
70.70	2.20	0.00	-12.65	0.00	-2.18	0.00	0.00	0.00	-0.02	12.84
71.42	2.24	0.00	-12.92	0.00	-2.23	0.00	0.01	0.00	-0.02	13.11
72.17	2.30	0.00	-13.20	0.00	-2.27	0.00	0.01	0.00	-0.02	13.40
72.94	2.33	0.00	-13.50	0.00	-2.31	0.00	0.00	0.00	-0.02	13.70
73.73	2.37	0.00	-13.81	0.00	-2.35	0.00	0.00	0.00	-0.02	14.01
74.53	2.39	0.00	-14.13	0.00	-2.37	0.00	0.00	0.00	-0.02	14.33
75.35	2.42	0.00	-14.46	0.00	-2.39	0.00	0.00	0.00	-0.02	14.66
76.19	2.43	0.00	-14.79	0.00	-2.41	0.00	0.00	0.00	-0.02	14.99
77.03	2.44	0.00	-15.13	0.00	-2.42	0.00	0.00	0.00	-0.02	15.33
77.90	2.44	0.00	-15.48	0.00	-2.42	0.00	0.00	0.00	-0.02	15.67
78.78	2.43	0.00	-15.83	0.00	-2.41	0.00	0.00	0.00	-0.02	16.02
79.66	2.41	0.00	-16.18	0.00	-2.39	0.00	0.00	0.00	-0.02	16.36
80.56	2.39	0.00	-16.54	0.00	-2.37	0.00	0.00	0.00	-0.02	16.71
81.46	2.36	0.00	-16.89	0.00	-2.34	0.00	0.00	0.00	-0.02	17.05
82.38	2.32	0.00	-17.24	0.00	-2.30	0.00	0.00	0.00	-0.02	17.39
83.30	2.27	0.00	-17.58	0.00	-2.26	0.00	0.00	0.00	-0.02	17.73
84.22	2.22	0.00	-17.92	0.00	-2.21	0.00	0.00	0.00	-0.02	18.06
85.15	2.17	0.00	-18.25	0.00	-2.15	0.00	0.00	0.00	-0.02	18.38
86.08	2.11	0.00	-18.57	0.00	-2.09	0.00	0.00	0.00	-0.02	18.69
87.03	2.04	0.00	-18.89	0.00	-2.03	0.00	0.00	0.00	-0.02	19.00
87.98	1.97	0.00	-19.20	0.00	-1.96	0.00	0.00	0.00	-0.01	19.30
88.93	1.91	0.00	-19.49	0.00	-1.89	0.00	0.00	0.00	-0.01	19.58
89.87	1.84	0.00	-19.77	0.00	-1.82	0.00	0.00	0.00	-0.01	19.86
90.82	1.77	0.00	-20.05	0.00	-1.75	0.00	0.00	0.00	-0.01	20.12
91.77	1.70	0.00	-20.31	0.00	-1.69	0.00	0.00	0.00	-0.01	20.38
92.72	1.63	0.00	-20.56	0.00	-1.62	0.00	0.00	0.00	-0.01	20.63
93.68	1.57	0.00	-20.80	0.00	-1.56	0.00	0.00	0.00	-0.01	20.86
94.63	1.52	0.00	-21.03	0.00	-1.50	0.00	0.00	0.00	-0.01	21.09
95.58	1.46	0.00	-21.25	0.00	-1.45	0.00	0.00	0.00	-0.01	21.30
96.54	1.41	0.00	-21.47	0.00	-1.40	0.00	0.00	0.00	-0.01	21.52
97.50	1.37	0.00	-21.68	0.00	-1.36	0.00	0.00	0.00	-0.01	21.72
98.47	1.33	0.00	-21.88	0.00	-1.32	0.00	0.00	0.00	-0.01	21.92
99.44	1.30	0.00	-22.07	0.00	-1.29	0.00	0.00	0.00	-0.01	22.11
100.40	1.28	0.00	-22.26	0.00	-1.26	0.00	0.00	0.00	-0.01	22.29
101.37	1.25	0.00	-22.44	0.00	-1.24	0.00	0.00	0.00	-0.01	22.47
102.32	1.23	0.00	-22.61	0.00	-1.21	0.00	0.00	0.00	-0.02	22.65
103.28	1.21	0.00	-22.78	0.00	-1.19	0.00	0.00	0.00	-0.01	22.82
104.23	1.18	0.00	-22.95	0.00	-1.16	0.00	0.00	0.00	-0.01	22.98
105.19	1.14	0.00	-23.11	0.00	-1.12	0.00	0.00	0.00	-0.01	23.14
106.15	1.09	0.00	-23.27	0.00	-1.07	0.00	-0.01	0.00	-0.01	23.30
107.11	1.02	0.00	-23.42	0.00	-1.01	0.00	-0.01	0.00	-0.01	23.44
108.08	0.94	0.00	-23.56	0.00	-0.93	0.00	-0.01	0.00	-0.01	23.58
109.04	0.84	0.00	-23.70	0.00	-0.83	0.00	-0.01	0.00	-0.01	23.71
110.00	0.73	0.00	-23.81	0.00	-0.72	0.00	-0.01	0.00	0.00	23.83

Table B.5: Second invariant values at each point along h = -7.5 mm

Position along x (mm)	du/dx	du/dy	du/dz	dv/dx	dv/dy	dv/dz	dw/dx	dw/dy	dw/dz	S^2
70.00	1.53	0.00	15.92	0.00	-1.48	0.00	0.01	0.00	-0.03	15.99
70.70	1.54	0.00	16.27	0.00	-1.52	0.00	0.00	0.00	-0.03	16.34
71.42	1.57	0.00	16.63	0.00	-1.55	0.00	-0.01	0.00	-0.03	16.71
72.17	1.61	0.00	17.02	0.00	-1.58	0.00	0.00	0.00	-0.03	17.09
72.94	1.64	0.00	17.42	0.00	-1.61	0.00	0.00	0.00	-0.03	17.50
73.73	1.66	0.00	17.84	0.00	-1.63	0.00	0.00	0.00	-0.03	17.92
74.53	1.68	0.00	18.27	0.00	-1.65	0.00	0.00	0.00	-0.03	18.35
75.35	1.70	0.00	18.72	0.00	-1.67	0.00	0.00	0.00	-0.03	18.80
76.19	1.71	0.00	19.17	0.00	-1.68	0.00	0.00	0.00	-0.03	19.25
77.03	1.71	0.00	19.64	0.00	-1.68	0.00	0.00	0.00	-0.03	19.71
77.90	1.72	0.00	20.12	0.00	-1.69	0.00	0.00	0.00	-0.03	20.19
78.78	1.71	0.00	20.60	0.00	-1.68	0.00	0.00	0.00	-0.03	20.67
79.66	1.70	0.00	21.08	0.00	-1.67	0.00	0.00	0.00	-0.03	21.15
80.56	1.68	0.00	21.56	0.00	-1.66	0.00	0.00	0.00	-0.03	21.62
81.46	1.66	0.00	22.04	0.00	-1.64	0.00	0.00	0.00	-0.03	22.10
82.38	1.64	0.00	22.52	0.00	-1.61	0.00	0.00	0.00	-0.03	22.58
83.30	1.61	0.00	23.00	0.00	-1.58	0.00	0.00	0.00	-0.03	23.05
84.22	1.57	0.00	23.46	0.00	-1.55	0.00	0.00	0.00	-0.02	23.51
85.15	1.53	0.00	23.92	0.00	-1.51	0.00	0.00	0.00	-0.02	23.97
86.08	1.49	0.00	24.36	0.00	-1.47	0.00	0.00	0.00	-0.02	24.41
87.03	1.45	0.00	24.80	0.00	-1.42	0.00	0.00	0.00	-0.02	24.84
87.98	1.40	0.00	25.22	0.00	-1.38	0.00	0.00	0.00	-0.02	25.26
88.93	1.35	0.00	25.63	0.00	-1.33	0.00	0.00	0.00	-0.02	25.67
89.87	1.30	0.00	26.03	0.00	-1.29	0.00	0.00	0.00	-0.02	26.06
90.82	1.25	0.00	26.41	0.00	-1.24	0.00	0.00	0.00	-0.02	26.44
91.77	1.21	0.00	26.77	0.00	-1.19	0.00	0.00	0.00	-0.02	26.80
92.72	1.16	0.00	27.13	0.00	-1.15	0.00	0.00	0.00	-0.02	27.15
93.68	1.12	0.00	27.46	0.00	-1.10	0.00	0.00	0.00	-0.02	27.49
94.63	1.08	0.00	27.79	0.00	-1.07	0.00	0.00	0.00	-0.02	27.81
95.58	1.04	0.00	28.10	0.00	-1.03	0.00	0.00	0.00	-0.02	28.12
96.54	1.01	0.00	28.41	0.00	-1.00	0.00	0.00	0.00	-0.02	28.42
97.50	0.98	0.00	28.70	0.00	-0.97	0.00	0.00	0.00	-0.02	28.72
98.47	0.96	0.00	28.99	0.00	-0.94	0.00	0.00	0.00	-0.02	29.00
99.44	0.94	0.00	29.27	0.00	-0.92	0.00	0.00	0.00	-0.02	29.28
100.40	0.92	0.00	29.54	0.00	-0.90	0.00	0.00	0.00	-0.02	29.55
101.37	0.90	0.00	29.80	0.00	-0.89	0.00	0.00	0.00	-0.02	29.82
102.32	0.89	0.00	30.06	0.00	-0.87	0.00	0.00	0.00	-0.02	30.07
103.28	0.87	0.00	30.31	0.00	-0.85	0.00	0.00	0.00	-0.02	30.32
104.23	0.85	0.00	30.56	0.00	-0.83	0.00	0.00	0.00	-0.02	30.57
105.19	0.82	0.00	30.80	0.00	-0.81	0.00	0.00	0.00	-0.02	30.81
106.15	0.79	0.00	31.03	0.00	-0.77	0.00	0.00	0.00	-0.02	31.04
107.11	0.74	0.00	31.25	0.00	-0.72	0.00	0.01	0.00	-0.01	31.26
108.08	0.67	0.00	31.45	0.00	-0.66	0.00	0.01	0.00	-0.01	31.46
109.04	0.60	0.00	31.64	0.00	-0.59	0.00	0.01	0.00	-0.01	31.65
110.00	0.51	0.00	31.81	0.00	-0.51	0.00	0.01	0.00	0.00	31.81

Bibliography

[1] Lord Rayleigh, "On the Capillary Phenomena of Jets," *Proc. R. Soc. Lond.*, vol. 29, no. 196–199, pp. 71–97, Jan. 1879.

[2] G. I. Taylor, "The formation of emulsions in definable fields of flow," *Proc. R. Soc. Lond. A*, vol. 146, pp. 501–523, 1934.

[3] S. Tomatika, "On the instability of a cylindrical thread of a viscous liquid surrounded by another viscous fluid," *Proc. R. Soc. Lond. A*, vol. 150, pp. 322–337, 1935.

[4] H. P. Grace, "Dispersion phenomena in high viscosity immiscible fluid systems and application of static mixers as dispersion devices in such systems," *Chem. Eng. Commun.*, vol. 14, no. 3–6, pp. 225–277, 1982.

[5] Y. W. Stegeman, F. N. Van De Vosse, and H. E. H. Meijer, "On the applicability of the grace curve in practical mixing operations," *Can. J. Chem. Eng.*, vol. 80, no. 4, pp. 1–6, 2002.

[6] B. J. Bentley and L. G. Leal, "An experimental investigation of drop deformation and breakup in steady, two-dimensional linear flows," *J. Fluid Mech.*, vol. 167, pp. 241–283, 1986.

[7] J. M. Rallison, "The deformation of small viscous drops and bubbles in shear flows," *Annu. Rev. Fluid Mech.*, vol. 16, pp. 45–66, 1984.

[8] H. A. Stone, "Dynamics of drop deformation and breakup in viscous fluids," *Annu. Rev. Fluid Mech.*, vol. 26, pp. 65–102, 1994.

[9] C. R. Marks, "Drop breakup and deformation in sudden onset strong flows," Doctor of Philosophy, University of Maryland, College Park, Maryland, 20740, USA, 1998.

[10] H. A. Stone, B. J. Bentley, and L. G. Leal, "An experimental study of transient effects in the breakup of viscous drops," *J. Fluid Mech.*, vol. 173, pp. 131–158, 1986.

[11] R. G. Cox, "The deformation of drops in a general time dependent flow," *J. Fluid Mech.*, vol. 37, no. 3, pp. 601–623, Jul. 1969.

[12] J. D. Buckmaster, "Pointed bubbles in slow viscous flow," *J. Fluid Mech.*, vol. 55, no. 3, pp. 385–400, Oct. 1972.

[13] A. Acrivos and T. S. Lo, “Deformation and breakup of a single slender drop in an extensional flow,” *J. Fluid Mech.*, vol. 86, no. 4, pp. 641–672, 1978.

[14] J.-W. Ha and L. G. Leal, “An experimental study of drop deformation and breakup in extensional flow at high capillary number,” *Phys. Fluids 1994-Present*, vol. 13, no. 6, pp. 1568–1576, Jun. 2001.

[15] J. M. H. Janssen and H. E. H. Meijer, “Droplet breakup mechanisms: Stepwise equilibrium versus transient dispersion,” *J. Rheol.*, vol. 37, no. 4, pp. 597–608, Jul. 1993.

[16] H. B. Chin and C. D. Han, “Studies on droplet deformation and breakup 1: droplet deformation in extensional flow,” *J. Rheol.*, vol. 23, pp. 557–590, 1979.

[17] C. D. Han and K. Funatsu, “An experimental study of droplet deformation and breakup in pressure-driven flows through concerging and uniform channels,” *J. Rheol.*, vol. 22, pp. 113–133, 1978.

[18] F. D. Godbille and J. J. C. Picot, “Drop breakup in combined shear and extensional flow conditions,” *Adv. Polym. Technol.*, vol. 19, no. 1, pp. 14–21, 2000.

[19] D. Bourry, R. E. Khayat, L. A. Utracki, F. Godbille, J. Picot, and A. Luciani, “Extensional flow of polymeric dispersions,” *Polym. Eng. Sci.*, vol. 39, no. 6, pp. 1072–1086, Jun. 1999.

[20] M. S. N. Oliveira, M. A. Alves, F. T. Pinho, and G. H. McKinley, “Viscous flow through microfabricated hyperbolic contractions,” *Exp. Fluids*, vol. 43, no. 2–3, pp. 437–451, May 2007.

[21] M. K. Mulligan and J. P. Rothstein, “The effect of confinement-induced shear on drop deformation and breakup in microfluidic extensional flows,” *Phys. Fluids*, vol. 23, no. 2, p. 022004, Feb. 2011.

[22] T. Mikami, R. G. Cox, and S. G. Mason, “Breakup of extending liquid threads,” *Int. J. Multiph. Flow*, vol. 2, pp. 113–138, 1975.

[23] F. White, *Viscous fluid flow*, 2nd ed. New York: McGraw-Hill, 1991.